Complete NLO corrections to off-shell t̄tZ production at the LHC

Ansgar Denner,[a] **Daniele Lombardi**[a] **and Giovanni Pelliccioli**[b]

[a]*Institut für Theoretische Physik und Astrophysik, Universität Würzburg,*
Emil-Hilb-Weg 22, 97074 Würzburg, Germany

[b]*Max-Planck-Institut für Physik,*
Föhringer Ring 6, 80805 München, Germany

E-mail: ansgar.denner@physik.uni-wuerzburg.de,
daniele.lombardi@physik.uni-wuerzburg.de, gpellicc@mpp.mpg.de

ABSTRACT: Measuring precisely top-pair-associated processes at hadron colliders will become possible with the upcoming LHC running stages. The increased data statistics will especially enable differential measurements leading to an improved characterisation of such processes. Aiming at a consistent data-theory comparison, precise Standard-Model predictions are needed, including higher-order corrections and full off-shell effects. In this work we present NLO-accurate predictions for the production and decay of a top-antitop pair in association with a Z boson at the LHC, in the multi-lepton decay channel. The complete set of LO contributions and NLO corrections of EW and QCD origin is included. The calculation is based on full matrix elements, computed with all resonant and non-resonant contributions, complete spin correlations and interference effects. Integrated and differential cross-sections are presented for a realistic fiducial setup.

KEYWORDS: Higher Order Electroweak Calculations, Top Quark

ARXIV EPRINT: 2306.13535

Contents

1 Introduction

In view of the upcoming full Run-3 dataset and of the future high-luminosity stage of the Large Hadron Collider (LHC), the increasing level of precision of LHC experiments requires to be matched by theoretical predictions in the Standard Model (SM). An improved interpretation of the data will then lead to cutting-edge results either confirming the SM or highlighting new-physics effects. The increased luminosity will allow for precise measurements of rare signatures that are expected to unveil the interplay between the top-quark and electroweak (EW) sector of the SM. At the LHC, a direct access to the top-quark coupling to EW bosons is given by the measurement of the production of a top-quark pair in association with an EW boson, namely of the $t\bar{t}Z$ and $t\bar{t}W^\pm$ production processes. Such signals are characterised by a large number of particles in the final state and rather intricate resonance structures involving top quarks, W, Z, and Higgs bosons, such that a proper theoretical modelling is required at production and decay level.

The $t\bar{t}Z$ process admits access to the top-quark coupling to Z bosons, which is still poorly constrained by experimental measurements, leaving room for new-physics effects [1, 2]. This freedom has already been exploited in different beyond-the-SM (BSM) scenarios. For instance, anomalous values of the top-Z coupling can be interpreted in terms of the presence of top-philic resonances like Z′ [3–6] and vector-like leptons [7]. A number of studies on $t\bar{t}Z$ production has been performed in the presence of higher-dimension effective

operators [1, 2, 8–17]. It has been noticed [13, 18] that, similarly to the case of the $t\bar{t}W^{\pm}$ process, the production of $t\bar{t}Z$ in association with jets is enhanced by $tZ \to tZ$ and $bW \to tZ$ underlying scattering processes. In the presence of anomalous couplings between the top quark and EW bosons, this mechanism for $t\bar{t}Z$ production would lead to a unitarity-violating energy growth of the amplitude that must be regularised by new-physics mechanisms. Moreover, the $t\bar{t}Z$ process with the Z boson decaying into neutrinos represents a background to dark-matter LHC searches [19].

The ATLAS and CMS collaborations have measured $t\bar{t}Z$ production with Run-1 [20, 21] and Run-2 data [22–26]. The mostly considered decay channels are those involving three or four charged leptons, with at least two opposite-sign, same-flavour leptons. The four-lepton one, in spite of the lower decay branching fraction, has a very clean signature and a low background yield, thanks to the optimised lepton identification in ATLAS and CMS detectors. Like the $t\bar{t}W$ process, the $t\bar{t}Z$ one deserves high level of interest in the LHC community also because it represents one of the largest backgrounds to $t\bar{t}H$ production in the multi-lepton decay channel [27]. A proper modelling of $t\bar{t}Z$ production is therefore crucial for both $t\bar{t}V$ and $t\bar{t}H$ measurements.

In the context of SM modelling, the next-to-leading-order (NLO) QCD corrections to the $t\bar{t}Z$ process are known since many years [28, 29] for on-shell top quarks and Z bosons, while the subleading NLO corrections are more recent [30, 31]. The matching of NLO QCD corrections to parton shower (PS) has been performed with leading-order (LO) decays simulated in the narrow-width approximation for top quarks and Z bosons [27, 32, 33] and more recently including full off-shell effects related to the lepton pair from the Z-boson decay [34]. The NLO QCD corrections to the top-quark decays in $t\bar{t}Z$ production have also been computed in the narrow-width approximation [11]. Resummed calculations are available in the literature up to NLO+NNLL accuracy [35–38] in the case of on-shell resonances. For a realistic comparison with experimental data in fiducial setups, it is necessary to properly model the decay effects, with the possible inclusion of higher orders in perturbation theory. The need for precise off-shell predictions is urgent, given the recent measurement of differential cross-sections in angular and transverse-momentum observables [25, 26] with Run-2 data. The increased luminosity of the upcoming data will allow for an even more precise differential description of the process. The first off-shell calculation for the $t\bar{t}Z$ reaction at NLO QCD was performed for the Z boson decaying into neutrinos, with the purpose of modelling the sizeable QCD background in dark-matter searches [19]. An analogous calculation (at NLO QCD) has been recently presented in the four-charged-lepton decay channel [39].

In this work, we present SM predictions for the $t\bar{t}Z$ process that go one step forward in accuracy and modelling. In addition to the NLO QCD corrections to the leading tree-level process that were first computed in ref. [39], we calculate all subleading LO contributions and NLO corrections of EW and QCD type. All kinds of non-resonant contributions, spin correlations, and interferences are accounted for at LO and at NLO. Photon-induced and bottom-induced partonic channels are consistently included, giving a complete NLO calculation in the five-flavour scheme. At variance with ref. [30], we do not include heavy-boson radiation at NLO EW. Although these contributions typically account for a percent in inclusive setups, they are usually regarded as reducible backgrounds owing to a different final-state signature given by the additional heavy-boson decay products.

This article is structured as follows. In section 2 we detail our fixed-order calculation of the t̄tZ process, highlighting the most relevant theoretical aspects of EW and QCD corrections in the full off-shell description, the partonic channels that contribute in Born-like and real topologies, and the interplay between different perturbative orders. A comparison with existing results in the literature is presented in section 2.3. Our numerical results obtained in a realistic fiducial setup are shown in section 3, including integrated cross-sections and differential distributions in typical LHC observables. In section 4 we summarise the main achievements of the calculation and present our conclusions.

2 Details of the calculation

In this paper we present the complete set of NLO EW and NLO QCD corrections to the process

$$\mathrm{pp} \to \mathrm{e}^+ \nu_\mathrm{e}\, \mu^- \overline{\nu}_\mu\, \mathrm{b}\, \overline{\mathrm{b}}\, \tau^+ \tau^- \,. \tag{2.1}$$

The calculation has been performed with the in-house program MoCaNLO, a multichannel Monte Carlo generator that has already proven suitable for the evaluation of processes with high-multiplicity final states and involving top quarks at NLO QCD and NLO EW accuracy [40–45]. It is interfaced with Recola [46, 47], which provides the tree-level SM matrix elements together with the spin-correlated and colour-correlated ones, required for the definition of the unintegrated subtraction counterterms. Recola also computes all the required one-loop amplitudes using the Collier library [48] to perform the reduction and numerical evaluation of one-loop integrals [49–51].[1]

We explicitly calculate the process in eq. (2.1), whose final state involves three different lepton flavours. Despite that, predictions for leptons of the same flavour can be roughly recovered by multiplying our results by appropriate factors, which account for the number of identical particles in the final state. This procedure is expected to deliver the correct cross-section up to interference effects, which are known to have a marginal impact. Indeed, it has been shown in ref. [39] for the same hadronic process discussed here that differences in the LO QCD cross-section induced by the presence of same-flavour leptons are at the per-mille level for sufficiently inclusive cuts.

It is worth mentioning from the very beginning that in our setup for all diagrams involving a resonant Z boson the corresponding diagrams with photon-mediated contributions, as well as Z/γ^* interference effects, are properly taken into account. In ref. [39] it was also explicitly checked with a LO calculation that diagrams involving a Higgs boson, despite being quite numerous, contribute at the per-mille level and can be neglected to a first approximation. In our work all Higgs contributions are instead retained both in LO and in NLO terms. We also point out that throughout our calculation a diagonal quark-mixing matrix with unit entries is assumed.

---

[1] While Collier proved capable in calculating all required one-loop integrals for the practically relevant NLO corrections to the process (2.1), some improvements in the reduction of tensor integrals were required, in particular, for the reduction of rank-6 tensor integrals in 10-point functions appearing in the (very small) NLO corrections to the γg and γγ partonic processes.
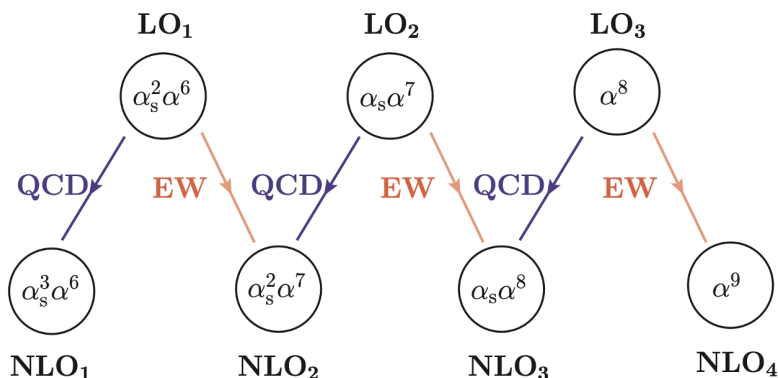
Figure 1. Perturbative orders contributing at LO and NLO for $t\bar{t}Z$ hadro-production in the four-charged-lepton channel.

2.1 Leading-order contributions

For the process (2.1) three LO contributions with different powers of α_s and α are allowed, if the possible partons initiating the reaction are not only selected from gluons (g) and light quarks ($q \in \{$u, d, s, c$\}$) but also from photons (γ) and bottom quarks (b), which are considered massless here. This is illustrated in figure 1, where the splitting and naming of the different contributions both for the LO and the NLO case make use of the notation proposed in refs. [31, 52].

The largest LO contribution originates from QCD-mediated partonic processes of order $\mathcal{O}(\alpha_s^2\alpha^6)$, which we dub LO_1. In this case, the colliding partons can be two gluons gg or a light quark-antiquark pair $q\bar{q}$, namely:

$$\text{gg} \rightarrow \text{e}^+\nu_{\text{e}}\,\mu^-\bar{\nu}_\mu\,\text{b}\,\bar{\text{b}}\,\tau^+\tau^- , \qquad q\bar{q} \rightarrow \text{e}^+\nu_{\text{e}}\,\mu^-\bar{\nu}_\mu\,\text{b}\,\bar{\text{b}}\,\tau^+\tau^- , \qquad (2.2)$$

where the gg partonic reaction alone requires the computation of roughly 2000 Feynman diagrams,[2] while each of the four[3] $q\bar{q}$ channels involves almost 1000 Feynman diagrams. Indeed, gluon-initiated reactions can proceed both via s-channel diagrams involving a triple-gluon coupling or t-channel diagrams, where the two incoming gluons are attached to a top- or bottom-quark line, as illustrated by sample diagrams in figure 2(a) and figure 2(b), respectively. In $q\bar{q}$-initiated reactions, an internal gluon always propagates in the s channel, like in the diagram shown in figure 2(c). Clearly, the gluon-induced channel represents the dominant contribution, due to the large gluon luminosity in the protons. Despite the large

---

[2]The approximate number of Feynman diagrams contributing at a given perturbative order is obtained from the one of integration channels provided by MOCANLO: even though the two numbers are not identical, their orders of magnitude match.

[3]Our counting is defined as follows: each channel with two different initial-state partons has to be computed separately for the two contributions differing by the interchange of the initial states. On the other hand, MOCANLO allows to compute together partonic reactions that differ by the exchange of the first and second generation of all initial-state light quarks, since the corresponding partonic amplitudes are identical and just need to be reweighted by appropriate PDF factors. Thus, in eq. (2.2) the four different $q\bar{q}$ channels to be calculated have the initial states u$\bar{\text{u}}$, $\bar{\text{u}}$u d$\bar{\text{d}}$, $\bar{\text{d}}$d.
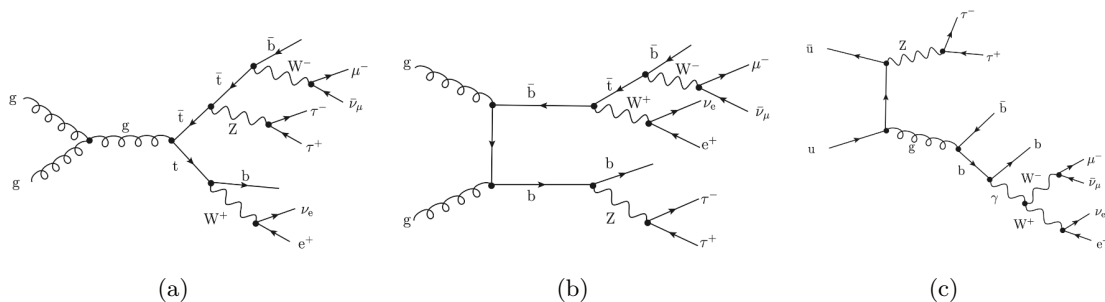
Figure 2. Sample LO_1 diagrams both in the gg and the $q\bar{q}$ channel with two [2(a)], one [2(b)], and zero [2(c)] top-quark resonances.
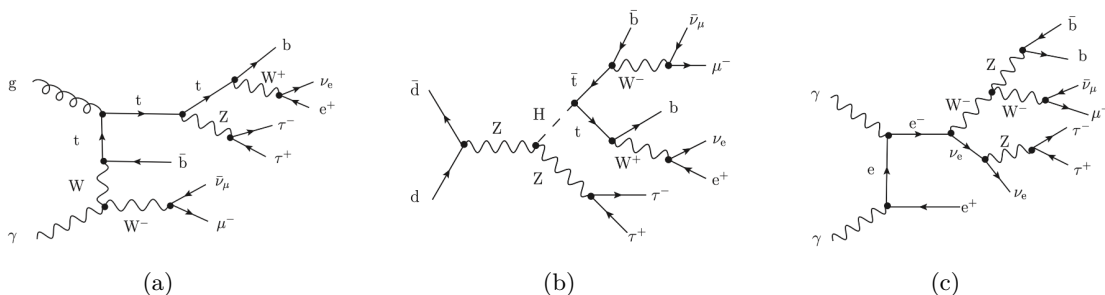

Figure 3. Sample LO_2 diagram for the γg channel with one top-quark resonance [3(a)] and LO_3 diagrams in the $q\bar{q}$ [3(b)] and $\gamma\gamma$ channel [3(c)] involving two and zero top-quark resonances, respectively.

number of diagrams, in both cases more than the 90% of the cross-section[4] originates from diagrams involving two resonant top quarks, either arising from an s-channel gluon splitting into a top-antitop pair or from a top-quark line directly attached to the incoming gluons (for the gg-initiated processes). Single-resonant and especially non-resonant top-quark diagrams have a much smaller impact if compared to the doubly-resonant ones.

At the order $\mathcal{O}(\alpha_s\alpha^7)$, labelled LO_2, as long as initial-state bottom quarks are excluded, the only non-zero contribution arises from the photon-gluon-induced partonic channel

$$\gamma g \rightarrow e^+\nu_e\,\mu^-\bar{\nu}_\mu\,b\,\bar{b}\,\tau^+\tau^- \,. \tag{2.3}$$

All other contributions at this perturbative order come from the interference between EW- and QCD-mediated quark-induced diagrams, which vanish owing to colour algebra. Despite the fact that the LO contribution from these channels is expected to be just a small fraction of the LO_1, due to the small photon luminosity, their calculation involves roughly 4000 Feynman diagrams. Moreover, the role of doubly-resonant top-quark topologies is not as dominant as for the LO_1 case: an equally important fraction of the result is ruled by single-resonant diagrams, which involve an incoming photon connected to the rest of the process by a γW^+W^- triple-gauge-boson vertex [like the one reported in figure 3(a)].

---

[4]The numerical impact of resonant and non-resonant contributions has been estimated by means of a survey of phase-space integration channels.
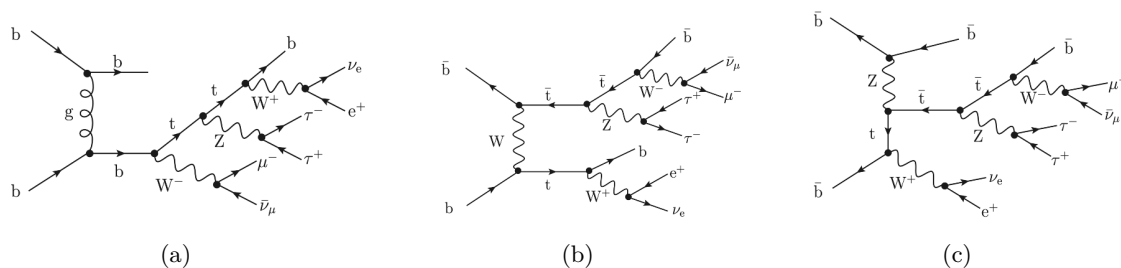
Figure 4. Sample LO$_1$ diagram for the bb bottom channel [4(a)] and LO$_3$ diagrams in the b$\bar{\text{b}}$ [4(b)] and $\bar{\text{b}}\bar{\text{b}}$ [4(c)] bottom channels.

Finally, an even smaller contribution originates from the fully EW-mediated processes, entering at order $\mathcal{O}(\alpha^7)$, that we refer to as LO$_3$ term. Due to the suppression caused by the small ratio of the α and the α_{s} couplings, this contribution is expected to amount to roughly 1% of the LO$_1$. In addition to the $q\bar{q}$-initiated partonic reactions, sharing the same external particles as its LO$_1$ counterpart in eq. (2.2) (but involving now only EW interaction vertices), the $\gamma\gamma$-induced channel also participates in the process through the reaction

$$\gamma\gamma \to \text{e}^+\nu_{\text{e}}\,\mu^-\bar{\nu}_\mu\,\text{b}\,\bar{\text{b}}\,\tau^+\tau^- \,. \tag{2.4}$$

In comparison with the $q\bar{q}$ channels, the $\gamma\gamma$ one represents just a tiny fraction of the overall LO$_3$ result, as a consequence of the additional suppression from the photon parton-distribution functions (PDFs). In spite of a negligible numerical impact, the EW nature of these processes allows for a very high number of topologies, involving approximately 6000 Feynman diagrams for $q\bar{q}$ channels and 17000 Feynman diagrams for the photon-initiated ones, where resonant and non-resonant configurations play an equally important role. Sample Feynman diagrams in the two configurations contributing at LO$_3$ are shown in figures 3(b) and 3(c).

Throughout our calculation, we made use of a five-flavour scheme, where the bottom quarks are treated as massless. Within this scheme, a consistent calculation should also include bottom-induced processes. The small value of the bottom PDFs is expected to highly suppress these contributions, as explicitly confirmed by a computation carried out in ref. [53] for t$\bar{\text{t}}$H production. Nevertheless, we decided to carry out their calculation for the t$\bar{\text{t}}$Z process consistently at all LO and NLO orders. Having a quantitative control on bottom-induced contributions is especially relevant in the calculation we present, because the size of the bottom-quark channels may become comparable to some of the subleading NLO corrections to the corresponding light-quark ones.

Customary b-jet taggings are charge blind, which means that bottom- and antibottom-initiated jets are not distinguished and have to be treated on the same footing. Therefore, already at LO additional partonic channels are present on top of the b$\bar{\text{b}}$ ones, namely the bb and $\bar{\text{b}}\bar{\text{b}}$ reactions,

$$\text{b}\bar{\text{b}} \to \text{e}^+\nu_{\text{e}}\,\mu^-\bar{\nu}_\mu\,\text{b}\,\bar{\text{b}}\,\tau^+\tau^- \,,$$
$$\text{bb} \to \text{e}^+\nu_{\text{e}}\,\mu^-\bar{\nu}_\mu\,\text{b}\,\text{b}\,\tau^+\tau^- \,, \qquad \bar{\text{b}}\bar{\text{b}} \to \text{e}^+\nu_{\text{e}}\,\mu^-\bar{\nu}_\mu\,\bar{\text{b}}\,\bar{\text{b}}\,\tau^+\tau^- \,. \tag{2.5}$$

The LO terms for the bottom channels contributing at $\mathcal{O}(\alpha_s^2 \alpha^6)$ (from now on $\mathrm{LO}_{b,1}$) require a computation of roughly 2000 Feynman diagrams for each partonic process. The $b\bar{b}$ channels are expected to dominate the LO_1 cross-section, since they mainly receive contributions from doubly-resonant diagrams; the $bb/\bar{b}\bar{b}$ bottom channels are instead resonance-suppressed, since only single or non-resonant topologies with a t-channel gluon exchange can contribute, as shown in figure 4(a).

At the order $\mathcal{O}(\alpha_s \alpha^7)$, named $\mathrm{LO}_{b,2}$, differently from the light-quark mediated case, non-vanishing contributions result from bottom-initiated reactions, both for the $b\bar{b}$ and the $bb/\bar{b}\bar{b}$ ones. For instance, for the $b\bar{b}$ case non-vanishing contributions arise by interfering EW tree-level diagrams with a t-channel W boson [as the one in figure 4(b)] and QCD ones with an s-channel gluon, and vice versa EW tree-level diagrams with an s-channel photon or Z boson and QCD ones with a t-channel gluon. For the $bb/\bar{b}\bar{b}$ case no s-channel topologies are allowed both for EW and QCD diagrams. Nevertheless, due to the presence of identical bottom quarks in the final state non-vanishing terms still emerge by interfering t-channel QCD diagrams [as the one in figure 4(a)] and u-channel EW ones, and vice versa.

Finally, we have also included the bottom channels at the order $\mathcal{O}(\alpha^8)$ or $\mathrm{LO}_{b,3}$. This computation requires to deal with approximately 11000 Feynman diagrams for each contribution in eq. (2.5), where the same channels now involve only EW interaction vertices. Besides configurations obtained by replacing a gluon with a neutral EW boson in a given $\mathrm{LO}_{b,1}$ diagram, a new class of reactions appears at this order. This contains Feynman diagrams involving a t-channel EW boson exchange like those reported in figure 4(b), where a W-mediated scattering between a b-quark and a $\bar{b}$-quark takes place, and in figure 4(c), which illustrates a $\bar{b}$-quark and an antitop-quark scattering via a Z boson exchange.

2.2 Next-to-leading-order corrections

As summarised in figure 1, NLO corrections to the $t\bar{t}Z$ process can be classified in four different categories, according to the perturbative order they contribute to. Pure QCD corrections enter at order $\mathcal{O}(\alpha_s^3 \alpha^6)$ and are denoted by NLO_1 contributions, followed by NLO_2 and NLO_3 corrections entering at the orders $\mathcal{O}(\alpha_s^2 \alpha^7)$ and $\mathcal{O}(\alpha_s \alpha^8)$, respectively, and finally pure EW corrections, dubbed NLO_4, which contribute at order $\mathcal{O}(\alpha^9)$. Perturbative corrections to the bottom-induced LO contributions will be occasionally referred to as $\mathrm{NLO}_{b,1}$, $\mathrm{NLO}_{b,2}$, $\mathrm{NLO}_{b,3}$, and $\mathrm{NLO}_{b,4}$, respectively.

Both QCD and QED singularities of infrared and collinear origin that plague the real contributions are treated using the dipole subtraction formalism [54–57]. The initial-state collinear singularities are absorbed in the PDFs in the $\overline{\mathrm{MS}}$ factorisation scheme.

Throughout our calculation, the complex-mass scheme for all unstable particles is used [58–61], resulting in complex input values for the EW boson masses, the top-quark mass, and the EW mixing angle,

$$\mu_V^2 = M_V^2 - i\Gamma_V M_V \quad (V = \mathrm{W}, \mathrm{Z}), \qquad \mu_t^2 = m_t^2 - i\Gamma_t m_t, \qquad \cos^2\theta_w = \frac{\mu_W^2}{\mu_Z^2}. \qquad (2.6)$$

– 7 –

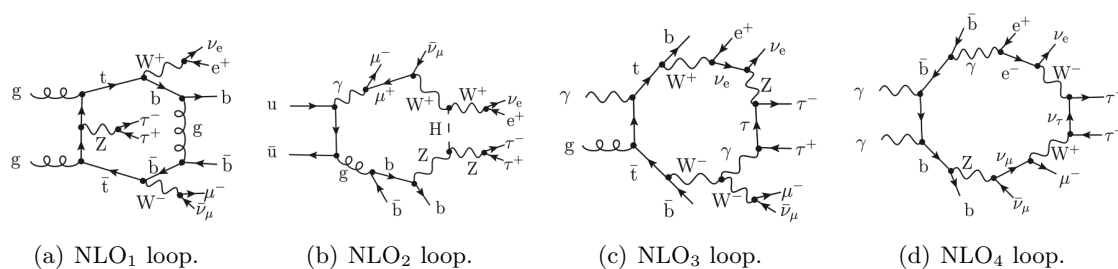|			
(a) NLO$_1$ loop.	(b) NLO$_2$ loop.	(c) NLO$_3$ loop.	(d) NLO$_4$ loop.

Figure 5. Sample one-loop diagrams involving loop functions of different complexity: 7-point, rank-6 loop functions for the gg channel entering at NLO$_1$ [5(a)]; 8-point, rank-3 loop functions for the $q\bar{q}$ channel entering at NLO$_2$ [5(b)]; 9-point, rank-5 loop functions for the γg channel entering at NLO$_3$ [5(c)]; 10-point, rank-6 loop functions for the $\gamma\gamma$ channel entering at NLO$_4$ [5(d)].

2.2.1 Contributions of order $\mathcal{O}(\alpha_\mathrm{s}^3\alpha^6)$

The QCD corrections to LO$_1$ give by far the largest NLO contribution. The real corrections originate from 13 different partonic processes (according to the counting explained in footnote 3), which can be summarised in the following reactions,

$$
\begin{aligned}
\mathrm{gg} &\to \mathrm{e}^+\nu_\mathrm{e}\,\mu^-\bar{\nu}_\mu\,\mathrm{b}\,\bar{\mathrm{b}}\,\tau^+\tau^-\mathrm{g}\,, & q\bar{q} &\to \mathrm{e}^+\nu_\mathrm{e}\,\mu^-\bar{\nu}_\mu\,\mathrm{b}\,\bar{\mathrm{b}}\,\tau^+\tau^-\mathrm{g}\,, \\
\mathrm{g}\bar{q} &\to \mathrm{e}^+\nu_\mathrm{e}\,\mu^-\bar{\nu}_\mu\,\mathrm{b}\,\bar{\mathrm{b}}\,\tau^+\tau^-\bar{q}\,, & \mathrm{g}q &\to \mathrm{e}^+\nu_\mathrm{e}\,\mu^-\bar{\nu}_\mu\,\mathrm{b}\,\bar{\mathrm{b}}\,\tau^+\tau^-q\,.
\end{aligned}
\tag{2.7}
$$

Owing to the large gluon luminosity, a considerable fraction of real corrections is due to the first partonic channel, which, together with the $q\bar{q}$ channel, is the one characterised by the largest number of IR singularities. The evaluation of the gg-initiated real channel is particularly challenging from a computational viewpoint, both for its large numerical contribution and for the higher number of integration channels compared to the $q\bar{q}$ real one. The calculation of the virtual corrections requires the evaluation of up to 7-point loop functions, having at most rank-4 and rank-6 for the $q\bar{q}$ and the gg case, respectively. Owing to the presence of the gg channel, loop diagrams involving 7-point functions can also occur for doubly-resonant topologies [see for instance figure 5(a)], as opposed to the t$\bar{\mathrm{t}}$W case [41]. Since the NLO$_1$ contribution to the t$\bar{\mathrm{t}}$Z process was already computed in ref. [39] within the HELAC-NLO framework [62], we have benefited from this calculation and, as a first step, we reproduced these corrections with MoCaNLO. We compared our results with the ones of ref. [39] finding very good agreement, as shown and further discussed in section 2.3.

At this perturbative order we have also included for the first time the QCD corrections to the LO$_{\mathrm{b},1}$ contribution, whose real part comprises 8 partonic contributions to be calculated with the following channels,

$$
\begin{aligned}
\mathrm{b}\bar{\mathrm{b}} &\to \mathrm{e}^+\nu_\mathrm{e}\,\mu^-\bar{\nu}_\mu\,\mathrm{b}\,\bar{\mathrm{b}}\,\tau^+\tau^-\mathrm{g}\,, \\
\mathrm{b}\mathrm{b} \to \mathrm{e}^+\nu_\mathrm{e}\,\mu^-\bar{\nu}_\mu\,\mathrm{b}\,\mathrm{b}\,\tau^+\tau^-\mathrm{g}\,, \qquad
\bar{\mathrm{b}}\bar{\mathrm{b}} &\to \mathrm{e}^+\nu_\mathrm{e}\,\mu^-\bar{\nu}_\mu\,\bar{\mathrm{b}}\,\bar{\mathrm{b}}\,\tau^+\tau^-\mathrm{g}\,, \\
\mathrm{g}\bar{\mathrm{b}} \to \mathrm{e}^+\nu_\mathrm{e}\,\mu^-\bar{\nu}_\mu\,\mathrm{b}\,\bar{\mathrm{b}}\,\tau^+\tau^-\bar{\mathrm{b}}\,, \qquad
\mathrm{g}\mathrm{b} &\to \mathrm{e}^+\nu_\mathrm{e}\,\mu^-\bar{\nu}_\mu\,\mathrm{b}\,\bar{\mathrm{b}}\,\tau^+\tau^-\mathrm{b}\,,
\end{aligned}
\tag{2.8}
$$

where the gb/g$\bar{\mathrm{b}}$-initiated ones involve three bottom quarks in the final state. The related diagrams include additional collinear singularities as compared to the ones in eq. (2.7),
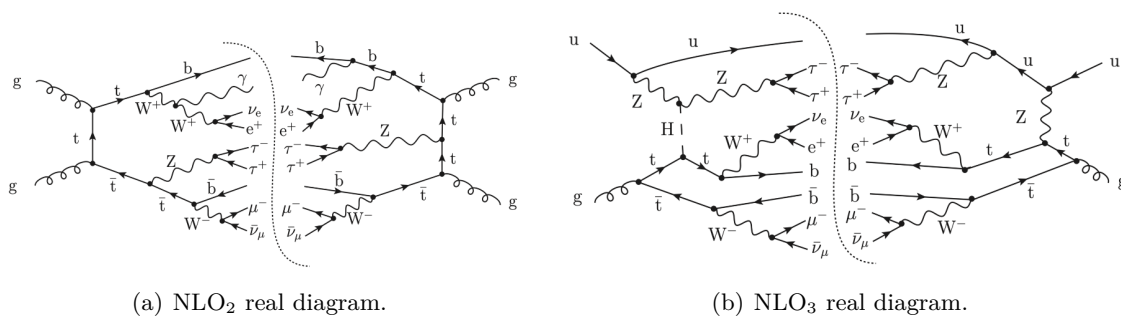
(a) NLO$_2$ real diagram. (b) NLO$_3$ real diagram.

Figure 6. A sample real squared diagram contributing at NLO$_2$ [6(a)], obtained as an EW correction to LO$_1$, and a sample squared diagram contributing at NLO$_3$ [6(b)], showing a tZ-scattering topology, representing a QCD correction to LO$_3$.

due to a gluon splitting into a b$\bar{\text{b}}$ pair. Nevertheless, these singularities do not need to be subtracted by introducing a dedicated subtraction term, since a t$\bar{\text{t}}$Z signature requires at least two resolved b jets in the final state that survive the fiducial cuts. Therefore, configurations involving two collinear b quarks are simply cut away if recombination rules that cluster two b jets into a light one are enforced as part of the jet-clustering algorithm, as further described in section 3.1 in eq. (3.5).

2.2.2 Contributions of order $\mathcal{O}(\alpha_s^2 \alpha^7)$

The NLO$_2$ corrections to the process (2.1) are the result of two different types of contributions, as shown pictorially in figure 1: EW corrections to LO$_1$ and QCD corrections to LO$_2$.

This distinction does not lead to any ambiguity for the real part of the calculation, where all squared diagrams can be attributed to one of the two contributions. Real EW corrections to the LO$_1$ term are characterised by the presence of an additional photon, either as an initial-state parton or as a final-state particle, as summarised in the following reactions,

$$
\begin{aligned}
\text{gg} &\to \text{e}^+\nu_\text{e}\,\mu^-\bar{\nu}_\mu\,\text{b}\,\bar{\text{b}}\,\tau^+\tau^-\gamma\,, & q\bar{q} &\to \text{e}^+\nu_\text{e}\,\mu^-\bar{\nu}_\mu\,\text{b}\,\bar{\text{b}}\,\tau^+\tau^-\gamma\,, \\
\gamma\bar{q} &\to \text{e}^+\nu_\text{e}\,\mu^-\bar{\nu}_\mu\,\text{b}\,\bar{\text{b}}\,\tau^+\tau^-\bar{q}\,, & \gamma q &\to \text{e}^+\nu_\text{e}\,\mu^-\bar{\nu}_\mu\,\text{b}\,\bar{\text{b}}\,\tau^+\tau^- q\,.
\end{aligned}
\tag{2.9}
$$

The gg and $q\bar{q}$ channels are again the most CPU-intensive ones to evaluate, since they represent the most significant fraction of the NLO$_2$ corrections and comprise many more integration channels as the corresponding real QCD counterparts in eq. (2.7). Indeed, the final-state photon can be radiated both by quark and lepton lines, resulting in an even richer singularity structure. A sample gg squared diagram belonging to this class of corrections is shown in figure 6(a). Channels involving one initial-state photon, although they contribute to the same perturbative order, are highly suppressed by the photon PDF. A similar discussion applies to the real EW corrections to the LO$_{\text{b},1}$ contributions, which
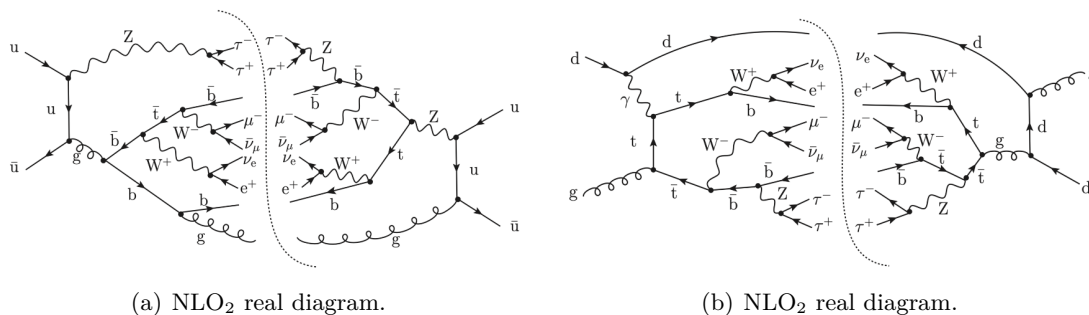
(a) NLO$_2$ real diagram.
(b) NLO$_2$ real diagram.

Figure 7. Sample real interference diagrams contributing at NLO$_2$ representing QCD corrections to LO$_2$ interference terms.

are characterised by the following reactions:

$$b\bar{b} \to e^+\nu_e\,\mu^-\bar{\nu}_\mu\,b\,\bar{b}\,\tau^+\tau^-\gamma\,,$$
$$bb \to e^+\nu_e\,\mu^-\bar{\nu}_\mu\,b\,b\,\tau^+\tau^-\gamma\,, \qquad \bar{b}\bar{b} \to e^+\nu_e\,\mu^-\bar{\nu}_\mu\,\bar{b}\,\bar{b}\,\tau^+\tau^-\gamma\,,$$
$$\gamma\bar{b} \to e^+\nu_e\,\mu^-\bar{\nu}_\mu\,b\,\bar{b}\,\tau^+\tau^-\bar{b}\,, \qquad \gamma b \to e^+\nu_e\,\mu^-\bar{\nu}_\mu\,b\,\bar{b}\,\tau^+\tau^-b\,. \tag{2.10}$$

The second class of real contributions arises from the QCD corrections to LO$_2$, obtained by interfering a tree-level LO$_1$ with a tree-level LO$_3$ diagram, with an additional QCD radiation exchange amongst the two. We notice that, even if the LO$_2$ is zero for the gg and $q\bar{q}$ channels due to colour algebra, the interference of the corresponding QCD-real amplitudes is non-vanishing if the gluon is exchanged between an initial quark or gluon and a final b-quark line of the two interfering diagrams, as in figure 7(a). Moreover, an additional interference contribution is permitted for gq and g$\bar{q}$ channels, where a quark line connects a genuinely QCD diagram with its EW counterpart, like in figure 7(b). Finally, real QCD corrections to LO$_2$ contributions, which are already non-zero at leading order, i.e. LO$_{b,2}$ and γg-initiated ones, are taken properly into account. For the latter the following real reaction has to be considered:

$$\gamma g \to e^+\nu_e\,\mu^-\bar{\nu}_\mu\,b\,\bar{b}\,\tau^+\tau^-g\,. \tag{2.11}$$

The neat distinction between the two classes of NLO$_2$ contributions is not possible anymore when considering the virtual corrections, as already pointed out in refs. [41, 43]. Indeed, interference of one-loop amplitudes of order $\mathcal{O}(g_s^4 g^6)$, obtained from the insertion of a gluon propagator in a QCD-mediated diagram, with tree-level EW diagrams of order $\mathcal{O}(g^8)$ are unambiguously classified as QCD corrections to LO$_2$, as shown in figure 8(a). But, for instance, the interference of one-loop amplitudes of order $\mathcal{O}(g_s^2 g^8)$ and tree-level QCD ones of order $\mathcal{O}(g_s^2 g^6)$ can either be considered as an EW correction to LO$_1$ or a QCD correction to LO$_2$. These terms are obtained by inserting an EW-particle propagator anywhere in a LO$_1$ squared amplitude [see for instance figure 8(b)]. This ambiguity is also reflected in the IR structure of this class of loop diagrams, whose singularities are fully cancelled only once contributions from both classes of real corrections are taken into account. Already for NLO$_2$ virtual contributions, the evaluation of loop integrals involving
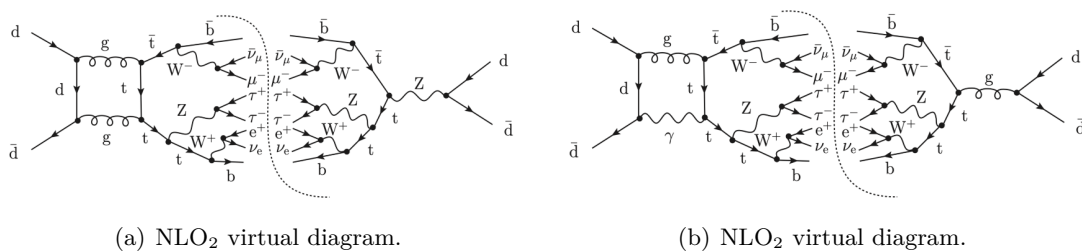
(a) NLO₂ virtual diagram.　　　　　　　　(b) NLO₂ virtual diagram.

Figure 8. Sample virtual interference diagrams contributing at NLO_2: the virtual diagram [8(a)] is uniquely identified as a QCD correction to an interference term; the virtual diagram [8(b)] can be considered both as an EW correction to a LO_1 amplitude and as a QCD correction to an interference contribution.

EW particles becomes extremely challenging due to the higher number of loop diagrams to account for and to the complexity of the loop integrals, which can involve up to 10-point functions with a maximal rank of 6, as in the gg channel, where two external vector bosons are attached to the loop. In figure 5(b) a sample NLO_2 diagram involving the computation of 8-point, rank-3 loop functions illustrates how the number of loop diagrams to be evaluated grows when EW particles are allowed to run in the loop, because of the larger number of topologies permitted.

2.2.3　Contributions of order $\mathcal{O}(\alpha_s \alpha^8)$

The largest part of the NLO_3 contribution arises from the QCD corrections to the LO_3 terms. The real-emission diagrams are obtained by adding an external gluon (either as initial or final state) to LO_3 amplitudes:

$$\gamma\gamma \to e^+ \nu_e \, \mu^- \bar{\nu}_\mu \, b\, \bar{b}\, \tau^+ \tau^- g\,, \qquad q\bar{q} \to e^+ \nu_e \, \mu^- \bar{\nu}_\mu \, b\, \bar{b}\, \tau^+ \tau^- g\,,$$
$$g\bar{q} \to e^+ \nu_e \, \mu^- \bar{\nu}_\mu \, b\, \bar{b}\, \tau^+ \tau^- \bar{q}\,, \qquad gq \to e^+ \nu_e \, \mu^- \bar{\nu}_\mu \, b\, \bar{b}\, \tau^+ \tau^- q\,, \qquad (2.12)$$

and similarly for the bottom-initiated contributions, where reactions with the same external particles like the ones in eq. (2.8) are found. Clearly, all channels are EW mediated: the only QCD vertex is the one at which the external gluon is attached. In line with the observation in ref. [41] for the $t\bar{t}W^\pm$ process, we also expect NLO_3 corrections to $t\bar{t}Z$ not to be negligible with respect to the NLO_2 ones. Indeed, even though these contributions are suppressed by an α/α_s factor, the real $g\bar{q}/gq$ channels embed a top-quark scattering against a Z boson [as shown in the left sub-diagram in figure 6(b)]. Their contribution is larger than the corresponding LO_3 and the largest of all NLO_3 corrections, as explicitly shown and further discussed in section 3.2. Conversely, we do not expect similar effects for the $g\bar{b}/gb$ reactions. Apart from the enhancement by the gluon PDFs, which still renders these partonic channels sizeable real $NLO_{b,3}$ corrections, no additional enhancement with respect to $LO_{b,3}$ due to the opening up of new topologies occurs in this case. Indeed, diagrams including a t-channel scattering of bottom quarks mediated by a W boson, which are the dominant topologies at NLO_3, are already present at $LO_{b,3}$, as exemplified by figure 4(b). Despite the larger number of diagrams, which is due to the EW nature of the process,
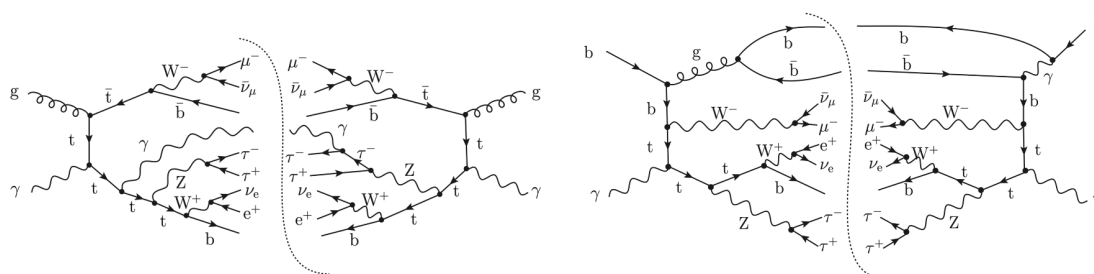
(a) NLO$_3$ real diagram for the γg channel.

(b) NLO$_3$ real diagram for the bottom contribution.

Figure 9. Sample real squared diagrams contributing at NLO$_3$ representing EW corrections to LO$_2$ for the γg channel [9(a)] and the bottom interference terms [9(b)].

the complexity of the loop functions to be evaluated for the QCD corrections to LO$_3$ is comparable to the one encountered for the NLO$_1$ case.

An additional class of corrections contributing at order $\mathcal{O}(\alpha_{\mathrm{s}}\alpha^8)$ results from EW corrections to LO$_2$, which are non-vanishing only for those terms whose LO$_2$ is already different from zero, since EW corrections do not modify the colour structure of the LO amplitude. That means that only EW corrections to the γg-initiated channel and to LO$_{\mathrm{b},2}$ have to be taken into account. For the γg channel, the real reaction [diagrammatically shown in figure 9(a)],

$$\gamma\mathrm{g} \to \mathrm{e}^+\nu_{\mathrm{e}}\,\mu^-\bar{\nu}_\mu\,\mathrm{b}\,\bar{\mathrm{b}}\,\tau^+\tau^-\gamma\,, \tag{2.13}$$

and the corresponding virtual term have to be computed. The latter turned out to be one of the most challenging virtual contributions to be evaluated within NLO$_1$, NLO$_2$, and NLO$_3$. Indeed, it requires the evaluation of 10-point functions up to rank 6, already encountered at NLO$_2$, but with a much larger number of topologies induced by the presence of a photon as initial-state parton. An exemplary NLO$_3$ loop diagram for this channel, involving up to 9-point, rank-5 loop functions is shown in figure 5(c). As far as the bottom contributions are concerned, real EW corrections are simply obtained by the emission of a photon off b$\bar{\mathrm{b}}$-, bb-, or $\bar{\mathrm{b}}\bar{\mathrm{b}}$-initiated QCD diagrams, which is then absorbed by an appropriate EW counterpart or by connecting a γb/$\bar{\gamma}$b-induced QCD diagram and its EW counterpart via a bottom-quark line [see for instance figure 9(b)]. As already found at NLO$_2$, the NLO$_3$ virtual contributions for the bottoms cannot be unambiguously separated into EW corrections to LO$_{\mathrm{b},2}$ and QCD corrections to LO$_{\mathrm{b},3}$. The interference of one-loop amplitudes of order $\mathcal{O}(g^{10})$ with tree-level diagrams of order $\mathcal{O}(g_{\mathrm{s}}^2 g^6)$ are uniquely identified as EW corrections to LO$_{\mathrm{b},2}$, as also clarified by figure 10(a). On the contrary, the interference of one-loop amplitudes of order $\mathcal{O}(g_{\mathrm{s}}^2 g^8)$ and tree-level ones of order $\mathcal{O}(g^8)$ can be attributed to both classes of corrections [see figure 10(b)].

2.2.4 Contributions of order $\mathcal{O}(\alpha^9)$

The NLO$_4$ contribution represents the last missing ingredient to furnish the full set of NLO corrections to t$\bar{\mathrm{t}}$Z production. As suggested by power counting and as explicitly shown in

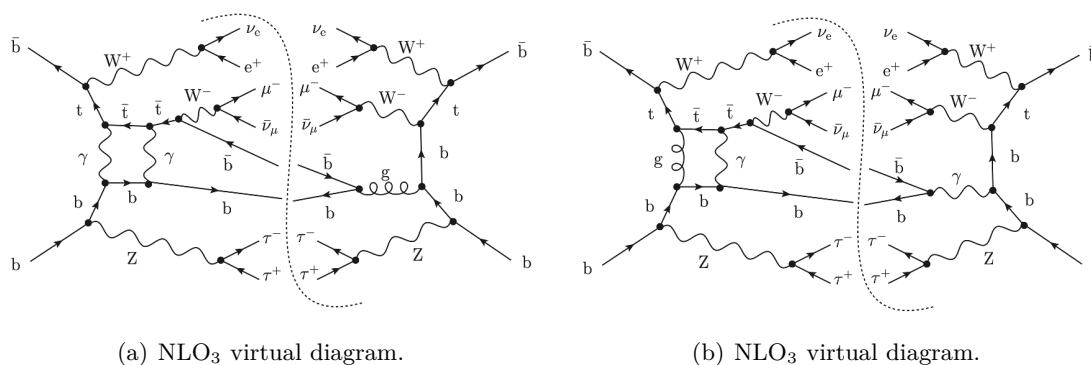(a) NLO$_3$ virtual diagram. (b) NLO$_3$ virtual diagram.

Figure 10. Sample virtual interference diagrams contributing at NLO$_3$ for the bottom channels: the virtual diagram [10(a)] is uniquely identified as an EW correction to an interference term; the virtual diagram [10(b)] can be considered both as a QCD correction to a LO$_3$ amplitude and as an EW correction to an interference contribution.

on-shell calculations [31], these corrections affect the overall result at the sub-per-mille level and are out of reach in any realistic measurement. The evaluation of these contributions requires to consider the set of real reactions

$$\gamma\gamma \to \mathrm{e}^+\nu_\mathrm{e}\,\mu^-\bar{\nu}_\mu\,\mathrm{b}\,\bar{\mathrm{b}}\,\tau^+\tau^-\gamma\,, \qquad q\bar{q} \to \mathrm{e}^+\nu_\mathrm{e}\,\mu^-\bar{\nu}_\mu\,\mathrm{b}\,\bar{\mathrm{b}}\,\tau^+\tau^-\gamma\,,$$
$$\gamma\bar{q} \to \mathrm{e}^+\nu_\mathrm{e}\,\mu^-\bar{\nu}_\mu\,\mathrm{b}\,\bar{\mathrm{b}}\,\tau^+\tau^-\bar{q}\,, \qquad \gamma q \to \mathrm{e}^+\nu_\mathrm{e}\,\mu^-\bar{\nu}_\mu\,\mathrm{b}\,\bar{\mathrm{b}}\,\tau^+\tau^- q\,, \qquad (2.14)$$

together with the bottom-induced ones as reported in eq. (2.10) but fully EW mediated. The bottleneck here is the numerical evaluation of virtual corrections. The most difficult term to be computed, which turns out to be also the least sizeable, is represented by the virtual EW corrections to the $\gamma\gamma$ channel: the presence of two external photons renders the number of 10-point, rank-6 loop functions to be evaluated even larger. A loop diagram involving loop functions of such a level of complexity is shown in figure 5(d) for the $\gamma\gamma$ initial state.

We present results for the NLO$_4$ contribution in a fully off-shell calculation for $t\bar{t}Z$ production at the integrated level for fiducial cross-sections in section 3.2, but we refrain from including them in any differential result.

2.3 Validation

Our calculation has been validated by reproducing NLO QCD results (LO$_1$ + NLO$_1$ in our notation) for fully off-shell $t\bar{t}Z$ production recently published in ref. [39] and obtained within the HELAC-NLO framework. Since those results have also been computed for a final state involving three different leptonic flavours, we just had to adapt our SM input parameters, presented in section 3.1, to the ones reported in ref. [39]. The most important features of the setup of ref. [39] that differ from those of our default setup and, thus, had to be readjusted for validation purposes are the following:

- the NLO top-quark width does not include NLO EW corrections;

- the factorisation and renormalisation scales are set to $\mu_0^{(c)}$, defined in eq. (3.9);

- different PDF sets are used for LO_1 and $LO_1 + NLO_1$ results (`NNPDF31_lo_as_0118` and `NNPDF31_nlo_as_0118`, respectively);

- no bottom-induced contributions are included.

Since the selection cuts used to generate our main results in section 3 (and described in section 3.1) match the ones in ref. [39], no additional adjustment to our calculation has been required.

In this setup we have obtained the following integrated cross-sections:

$$\sigma_{LO_1 \, nob} = 80.39(1)^{+25.54\,(32\%)}_{-18.03\,(22\%)}\,ab \quad \left(ref.\ [39]: 80.32^{+25.51\,(32\%)}_{-18.02\,(22\%)}\,ab\right),$$

$$\sigma_{NLO_1 \, nob} = 99.3(2)^{+1.25\,(1\%)}_{-5.83\,(6\%)}\,ab \qquad \left(ref.\ [39]: 98.88^{+1.22\,(1\%)}_{-5.68\,(6\%)}\,ab\right), \tag{2.15}$$

to be compared with eq. (4.3) of ref. [39] (reported here in parentheses as a reference). The digits in parentheses indicate the integration errors, while the absolute 7-point scale variations are reported as super-/sub-scripts with the respective relative variations as percentages in parenthesis. The agreement between the two LO_1 results is extremely good. The two central values differ at the 0.1% level, which confirms the size of Higgs-diagram contributions at LO_1 stated in ref. [39]. Indeed, the presence of Higgs contributions, included in our results, is an unavoidable difference between the two calculations. The theory uncertainty bands obtained via scale variations are also perfectly reproduced. A good agreement is found after including QCD corrections. In this case, although larger Monte Carlo uncertainties partially limit the comparison, the two results agree within $1.9\,\sigma$ (computed with the Monte Carlo error estimate of our result), which is more than satisfactory, especially considering the different treatment of Higgs diagrams that still persists at NLO.

The comparison with the calculation of ref. [39] has been carried out also at the differential level, by reproducing distributions in all kinematic variables reported therein. In all cases a good agreement was found, as confirmed by the selection of distributions in figure 11. We show the distribution in the azimuthal angle between the positron and the muon in figure 11(a) as well as the distributions in the transverse momentum of the $\tau^+\tau^-$ pair [figure 11(b)], of the subleading b jet [figure 11(c)], and of the positron [figure 11(d)]. In the main panels the LO_1 and $LO_1 + NLO_1$ results (with no bottom contributions included) are presented with a blue and red curve, respectively. In the ratio panels the same results normalised to the LO_1 one are reported. The corresponding distributions can be found in figures 6, 7, and 8 of ref. [39]. A direct comparison reveals that the relative NLO_1 corrections as well as the size of the QCD-uncertainty bands obtained with 7-point scale variations [see eq. (3.11)] are correctly reproduced by our calculation.
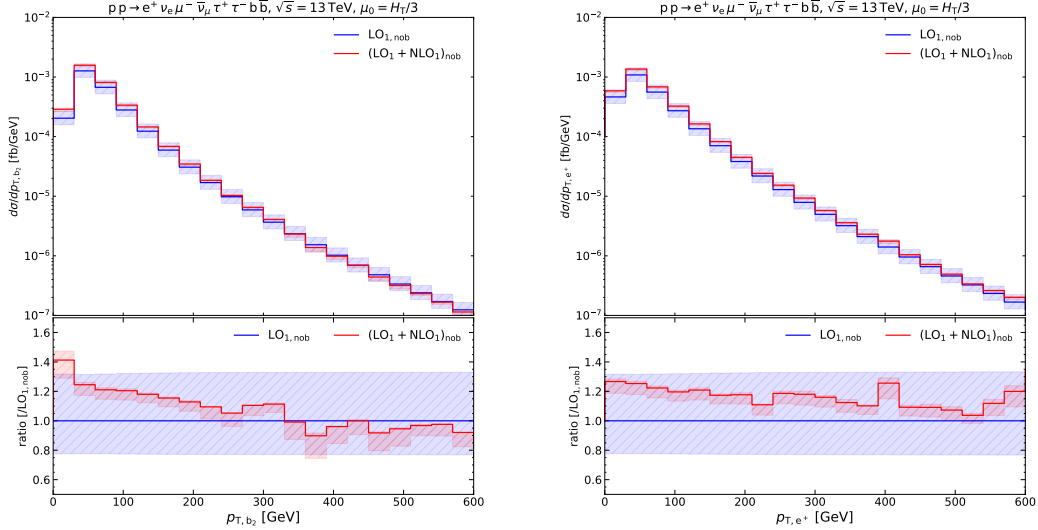
3 Numerical results

3.1 Input parameters

In the following, we present results for the LHC at a centre-of-mass energy of 13 TeV. We consider the process (2.1) with four different charged leptons in the final state. All leptons
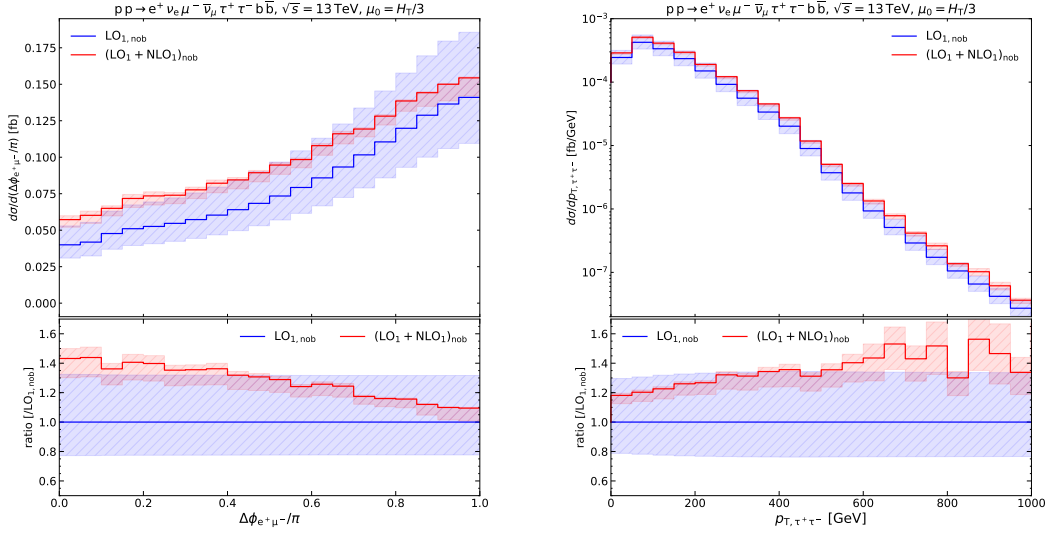
(a) Azimuthal-angle separation between the positron and the muon.

(b) Transverse momentum of the $\tau^+\tau^-$ pair.

(c) Transverse momentum of the subleading b jet.

(d) Transverse momentum of the positron.

Figure 11. Selected distributions used for validating our results against the ones obtained within the HELAC-NLO framework in ref. [39].

are assumed to be massless, i.e. also $m_\tau = 0$. We work in the five-flavour scheme, therefore we treat all light and bottom quarks as massless. A unit Cabibbo-Kobayashi-Maskawa matrix is understood.

The on-shell values for the masses and widths of the EW bosons are chosen according to [63],

$$
\begin{aligned}
M_{\mathrm{W}}^{\mathrm{OS}} &= 80.379\,\mathrm{GeV}, & \Gamma_{\mathrm{W}}^{\mathrm{OS}} &= 2.085\,\mathrm{GeV}\,, \\
M_{\mathrm{Z}}^{\mathrm{OS}} &= 91.1876\,\mathrm{GeV}, & \Gamma_{\mathrm{Z}}^{\mathrm{OS}} &= 2.4952\,\mathrm{GeV}\,, \\
M_{\mathrm{H}} &= 125\,\mathrm{GeV}, & \Gamma_{\mathrm{H}} &= 0.00407\,\mathrm{GeV}\,.
\end{aligned}
\tag{3.1}
$$

The masses of the vector bosons are converted to their pole values by means of the following relations [64]:

$$M_V = \frac{M_V^{\mathrm{OS}}}{\sqrt{1 + (\Gamma_V^{\mathrm{OS}}/M_V^{\mathrm{OS}})^2}}\,, \qquad \Gamma_V = \frac{\Gamma_V^{\mathrm{OS}}}{\sqrt{1 + (\Gamma_V^{\mathrm{OS}}/M_V^{\mathrm{OS}})^2}}\,. \tag{3.2}$$

The top-quark mass and width are fixed as

$$m_{\mathrm{t}} = 173.0\,\mathrm{GeV}\,, \qquad \Gamma_{\mathrm{t}}^{\mathrm{LO}} = 1.4437\,\mathrm{GeV}\,, \qquad \Gamma_{\mathrm{t}}^{\mathrm{NLO}} = 1.3636\,\mathrm{GeV}\,. \tag{3.3}$$

The top-quark width at LO has been computed with the formulas of ref. [65] and using the pole mass and width for the W boson as input. In order to meet the perturbative accuracy addressed in this work, the NLO width has been obtained upon applying QCD- and EW-correction factors from ref. [66] to the LO width. All LO and NLO results in sections 3.2 and 3.3 are obtained by using the NLO top-quark width in eq. (3.3).

The EW coupling is extracted from the Fermi constant G_μ by means of [67]

$$\alpha = \frac{\sqrt{2}}{\pi}\, G_\mu M_{\mathrm{W}}^2 \left(1 - \frac{M_{\mathrm{W}}^2}{M_{\mathrm{Z}}^2} \right)\,, \tag{3.4}$$

where $G_\mu = 1.16638 \cdot 10^{-5}\,\mathrm{GeV}^{-2}$.

The masses of unstable particles, i.e. the EW vector bosons and the top quark, are treated in the complex-mass scheme [58–61] in all parts of the computation. As a consequence, the EW mixing angle and the related couplings are complex valued.

For both the LO and the NLO calculation, we use `NNPDF31_nlo_as_0118_luxqed` PDFs [68, 69] extracted at NLO with $\alpha_{\mathrm{s}}(M_{\mathrm{Z}}) = 0.118$. The usage of this PDF set allows us to properly account for the photon PDF. The strong coupling constant α_{s} used in the calculation of the amplitudes matches the one used in the evolution of PDFs. The PDFs and the running of α_{s} are obtained by interfacing MoCaNLO with LHAPDF6 [70].

The QCD partons with pseudorapidity $|\eta| < 5$ are promoted to candidate jets and then used as inputs for the jet clustering performed with the anti-k_t algorithm [71] with resolution radius $R = 0.4$. As part of the jet clustering, we recombine a b jet and a light jet (j) into a b jet and two b jets into a light jet using the following recombination rules:

$$\mathrm{j} + \mathrm{j} \to \mathrm{j}, \qquad \mathrm{j_b} + \mathrm{j} \to \mathrm{j_b}, \qquad \mathrm{j_b} + \mathrm{j_b} \to \mathrm{j}, \tag{3.5}$$

where the last rule is crucial for bottom-induced contributions, which can include up to three bottoms in the final state, and where simply requiring two b jets does not remove all IR divergences (as discussed in section 2.1).

To facilitate the comparison of our results with the ones of ref. [39], we made use of the selection cuts of that paper, whose choice is motivated by a recent ATLAS analysis [26] (see table 2 therein) and a CMS one [25]. In particular, we ask for at least two b jets in the final state, assuming a perfect b-tagging efficiency, which are required to fulfil

$$p_{\mathrm{T,b}} > 25\,\mathrm{GeV}\,, \quad |\eta_{\mathrm{b}}| < 2.5\,, \quad \Delta R_{\mathrm{bb}} > 0.4\,. \tag{3.6}$$

Charged leptons are dressed with anti-k_t clustering algorithm, but with $R = 0.1$. For all charged leptons, we require

$$p_{\mathrm{T},\ell_i} > 20\,\mathrm{GeV}\,, \quad |\eta_{\ell_i}| < 2.5\,, \quad \Delta R_{\ell_i \ell_j} > 0.4\,, \tag{3.7}$$

where $\ell_i \in \{\mathrm{e}^+, \mu^-, \tau^+, \tau^-\}$. While these cuts are applied to the light leptons $\ell = \mathrm{e}, \mu$ by ATLAS, we apply them also to τ leptons. Finally, we apply a cut on the missing transverse momentum arising from the undetected neutrinos

$$p_{\mathrm{T,miss}} > 40\,\mathrm{GeV}\,, \tag{3.8}$$

where for the specific case at hand $p_{\mathrm{T,miss}}$ is computed as the transverse component of the sum of the momenta of the two neutrinos at Monte Carlo-truth level. No specific veto is imposed on the additional light- or b-jet activity that may arise as part of real QCD radiation at NLO.

As usual, we set the factorisation and renormalisation scales to the same central scale μ_0, i.e. $\mu_{\mathrm{R}} = \mu_{\mathrm{F}} = \mu_0$. For μ_0 we made use of two different choices. In order to directly compare our results with the ones of ref. [39], we adopted the following dynamical choice:

$$\mu_0^{(c)} = \frac{H_{\mathrm{T}}}{3} \quad \text{with} \quad H_{\mathrm{T}} = \sum_{i=1}^{2} p_{\mathrm{T,b}_i} + p_{\mathrm{T},\tau^+} + p_{\mathrm{T},\tau^-} + p_{\mathrm{T},\mu^-} + p_{\mathrm{T,e}^+} + p_{\mathrm{T,miss}}\,, \tag{3.9}$$

where the sum over the transverse momenta of the final states in H_{T} does not run over additional light jets. This scale has been adopted in section 2.3 to validate our calculation at NLO_1 level: since no bottom-induced channels are included for that comparison, the two b jets entering the definition of H_{T} are the only ones present in the partonic reaction. We notice that the definition in eq. (3.9) is insensitive to specific resonant topologies which lead to the final state of interest.

Our main results, discussed in sections 3.2 and 3.3, rely on a second scale choice, whose definition was first introduced in ref. [40] for $\mathrm{t\bar{t}W}^{\pm}$ production and which was in turn constructed in line with the choice of refs. [44, 45] for $\mathrm{t\bar{t}}$ and $\mathrm{t\bar{t}H}$ production:

$$\mu_0^{(d)} = \frac{1}{2} \left(M_{\mathrm{T,t}}\, M_{\mathrm{T,\bar{t}}} \right)^{1/2} = \frac{1}{2} \left(\sqrt{m_{\mathrm{t}}^2 + p_{\mathrm{T,t}}^2} \sqrt{m_{\mathrm{t}}^2 + p_{\mathrm{T,\bar{t}}}^2} \right)^{1/2}\,, \tag{3.10}$$

where the top and antitop transverse momenta are reconstructed from their decay products based on the Monte Carlo truth. As pointed out in ref. [40], since the determination of the top-quark momentum is subject to an ambiguity, we use the lepton-neutrino pair that, combined with the b quark, gives rise to an invariant mass which is the closest to m_{t}. This scale definition is physically motivated by the expectation that top-antitop resonant structures dominate the cross-section, even when considering off-shell effects. Moreover, the overall factor of one half in eq. (3.10) has been shown in ref. [40] to give a smaller scale sensitivity of the results when using the conventional 7-point scale variation and to reduce the size of QCD corrections (of NLO_1 type).

The uncertainties in our results are estimated by computing the 7-point scale envelope, i.e. by considering the maximum and minimum values of the cross-section evaluated on the

Channel	LO_1	LO_2	LO_3
gg	74.760(4)	-	-
$q\bar{q}$	32.486(3)	-	0.2848(1)
$b\bar{b}$	0.29208(9)	$-0.6330(2)$	0.7821(2)
$\bar{b}\bar{b}/bb$	0.02171(2)	0.002516(9)	0.005817(9)
γg	-	0.7522(2)	-
$\gamma\gamma$	-	-	0.001431(6)
sum	107.560(5)	0.1217(3)	1.0742(3)

Table 1. LO cross-sections (in ab) in the fiducial setup defined by eqs. (3.6)–(3.8) for the different sets of partonic channels contributing to the reaction $pp \rightarrow e^+\nu_e\,\mu^-\overline{\nu}_\mu\,b\,\overline{b}\,\tau^+\tau^-$. In the last line the sum of all partonic channels contributing at that specific order is reported as a reference. Integration errors are given in parentheses.

set of scales $(\mu_\mathrm{R},\,\mu_\mathrm{F})$ defined as

$$\left(\frac{\mu_\mathrm{R}}{\mu_0},\,\frac{\mu_\mathrm{F}}{\mu_0}\right) \in \left\{(0.5, 0.5),(0.5, 1),(1, 0.5),(1, 1),(2, 1),(1, 2),(2, 2)\right\}. \qquad (3.11)$$

Note that the α_s coupling entering the calculation of the NLO top-quark width is kept fixed for the evaluation of the scale envelope.

In the following two sections, we present results for the fiducial cross-sections and differential distributions where all contributions described in section 2 are combined in an *additive* scheme, i.e.

$$\sigma_{\mathrm{LO+NLO}} = \sigma_{\mathrm{LO}_1} + \sigma_{\mathrm{NLO}_1} + \sigma_{\mathrm{LO}_2} + \sigma_{\mathrm{NLO}_2} + \sigma_{\mathrm{LO}_3} + \sigma_{\mathrm{NLO}_3} + \sigma_{\mathrm{NLO}_4}, \qquad (3.12)$$

which provides an exact result at the order of truncation of the perturbative expansion.

3.2 Fiducial cross-sections

In this section we present results for the integrated cross-section at different levels of perturbative accuracy in the fiducial region discussed in section 3.1.

In table 1 we report the different LO contributions separately for the various partonic processes. Their sum at a given order is shown in the last line as a reference. As expected, the LO result is dominated by the contribution of the gg channel, which just enters at order $\mathcal{O}(\alpha_\mathrm{s}^2\alpha^6)$, due to the high luminosity of the gluon PDF. A significant fraction of the LO result is also represented by the $q\bar{q}$ channel, whose LO_1 is roughly 30% of the full LO_1 result. The $q\bar{q}$ partonic process enters also at LO_3, which only amounts to roughly 1% of the corresponding LO_1, as expected by the α/α_s power suppression. Its LO_2 (interference) contributions exactly vanish owing to colour algebra.

The $b\bar{b}$ and $bb/\bar{b}\bar{b}$ channels participate in all three LO terms, even though they contribute overall at the sub-percent level. The bottom contribution is dominated by the $b\bar{b}$ partonic channels, due to the enhancement of doubly-resonant top-quark topologies, which are absent for the $\bar{b}\bar{b}/bb$ cases. All LO contributions are comparable in size, contrary

Channel	NLO$_1$	NLO$_2$	NLO$_3$	NLO$_4$
gg	$-14.9(1)$	$-0.107(9)$	-	-
$q\bar{q}$	$-12.35(7)$	$-1.177(6)$	$0.013(4)$	$-0.0380(9)$
$b\bar{b}$	$-0.106(2)$	$0.253(2)$	$-0.324(4)$	$-0.0194(9)$
$\bar{b}\bar{b}/bb$	$0.00031(7)$	$-0.0017(1)$	$-0.0022(2)$	$-0.00059(2)$
γg	-	$-0.136(2)$	$0.0101(8)$	-
$\gamma\gamma$	-	-	$-0.00020(3)$	$-0.00010(2)$
$gq/g\bar{q}$	$15.77(3)$	$0.0570(5)$	$1.102(1)$	-
$gb/g\bar{b}$	$0.624(2)$	$-0.146(2)$	$0.237(2)$	-
$\gamma q/\gamma\bar{q}$	-	$0.4774(8)$	-	$0.00403(2)$
$\gamma b/\gamma\bar{b}$	-	$0.00347(9)$	$-0.00026(1)$	$0.00194(1)$
sum	$-10.9(1)$	$-0.78(1)$	$1.037(6)$	$-0.052(1)$

Table 2. NLO corrections (in ab) to the LO cross-section in the fiducial setup defined by eqs. (3.6)–(3.8) shown for the different sets of partonic channels contributing to the reaction $pp \to e^+\nu_e\,\mu^-\,\bar{\nu}_\mu\,b\,\bar{b}\,\tau^+\tau^-$. In the last line the sum of all partonic channels contributing at that specific order is reported as a reference. Integration errors are given in parentheses.

to the expectation from a naive power counting, with the interference terms in LO$_{b,2}$ having negative sign. Indeed, at $\mathcal{O}(\alpha^8)$ the $b\bar{b}$ partonic channel embeds doubly-resonant topologies with a t-channel W-boson exchange [like the one shown in figure 4(b)], which is absent in the corresponding tree-level QCD diagrams. Since the $bb/\bar{b}\bar{b}$ channels allow only for a single top resonance their integrated cross-sections are small fractions of the $b\bar{b}$ ones at each perturbative order: the largest $bb/\bar{b}\bar{b}$ contribution is provided by the LO$_{b,1}$ term, which is already only 7% of the LO$_{b,1}$ one for the $b\bar{b}$ channels.

Two additional partonic channels are allowed at LO, namely the γg and $\gamma\gamma$ ones. The former enters at $\mathcal{O}(\alpha_s\alpha^7)$ and is comparable in size with the contribution of the $b\bar{b}$ reactions: indeed the photon PDF suppression is partially compensated by the gluon PDF and by the appearence of topologies involving a t-channel W-boson exchange [as in figure 3(a)]. Overall, it amounts to roughly 1% of the contribution from the dominant gg channel. The purely photon-induced contributions are even further suppressed by the photon luminosity and by the EW nature of the reaction, accounting for a few milli-percent of the gg channel and for 0.1% of the full LO$_3$ result.

In table 2 we illustrate separately the contributions of the various partonic channels to the different NLO corrections. The sum of the channels at each perturbative order is reported in the last line as a reference. At NLO$_1$ the new gluon-induced partonic channels gq open up. In our fiducial setup they provide the largest correction in absolute value, which is of positive sign, since the gq channels just comprise real tree-level contributions (together with corresponding subtraction counterterms cancelling initial-state collinear singularities). The corresponding bottom counterparts, namely gb, are also present, but just amount to roughly 4% of the gq ones. A sizeable and negative correction at this order arises from

the virtual and real corrections to the gg and $q\bar{q}$ channels, roughly -20% and -38% of the corresponding LO_1, respectively. Similarly, for the $b\bar{b}$ process the $\text{LO}_{b,1}$ corrections amount to roughly -36% of the corresponding LO, but their contribution to the overall NLO_1 corrections is only about 1%. The QCD corrections to the $bb/\bar{b}\bar{b}$ bottom channels are instead fully negligible.

All partonic channels contributing to NLO_1 also receive corrections at the order together with the γg one, whose NLO_2 contribution can be unambiguously identified as a QCD correction to its LO_2. In our fiducial region the NLO_2 corrections to γg are negative and amount to -18% of their LO. At $\mathcal{O}(\alpha_s^2 \alpha^7)$ also the γq and γb channels open up, which are clearly EW real corrections to LO_1. Actually, the γq cross-section is the second-largest contribution (in absolute value) to NLO_2 after the one of the $q\bar{q}$ reaction. We remind the reader that the $q\bar{q}$ partonic channel, together with $b\bar{b}$, bb, and $\bar{b}\bar{b}$, receives both EW corrections from LO_1 and QCD corrections from LO_2, whose contributions cannot be unambiguously separated. The EW corrections to gg (also contributing at NLO_2 order) are quite small if compared to the corresponding NLO_1 ones (just a 0.8% of them). The real channels gq and gb enter at order $\mathcal{O}(\alpha_s^2 \alpha^7)$ as genuine QCD corrections to the LO interference. The NLO_2 result for the gq channel is 0.4% of its corresponding contribution at NLO_1, while for the gb one it amounts to 23% of the corresponding NLO_1 counterpart but of negative relative sign. More strikingly, the impact of the gb partonic channels is more sizeable than the gq one. This can be traced back to the different topologies contributing in the two cases. For gq initial states, the colour structure is only non-vanishing if the additional gluon connects the light-quark and the bottom-quark lines [see figure 7(a)]. In the gb case, the presence of t-channel gluon exchange in the LO QCD amplitude allows for more possibilities for the additional gluon to connect the two b-quark lines, opening diagram topologies with a non-vanishing colour factor that are not kinematically suppressed.

At NLO_3 the largest positive contribution comes from the gq channel, which plays the role of a QCD correction to LO_3, but is actually almost 4 times larger than the corresponding LO_3 cross-section in the $q\bar{q}$ channel. As anticipated in section 2.2.3, this result can be explained by the presence of tZ-scattering topologies that open up at this order [see left sub-diagram in figure 6(b)]. For the gb reaction, the NLO_3 contribution is a non-negligible fraction of its NLO_1 one, but roughly a factor of 3 smaller than the corresponding LO_3 cross-section in the $b\bar{b}$ channel. Indeed, differently from the gq case, all relevant scattering topologies contributing to the gb reaction are already present at $\text{LO}_{b,3}$. Therefore, the NLO_3 corrections to the $b\bar{b}$ channels are comparable in size to the gb ones, and, being negative, they largely cancel them. Moreover, since the $\text{LO}_{b,3}$ contribution is enhanced by EW-boson scattering topologies [see figures 4(b) and 4(c)], its QCD corrections to the $b\bar{b}$ and the $bb/\bar{b}\bar{b}$ channels are not suppressed with respect to the NLO_1 and NLO_2 corrections to the same channels. On the contrary, the $\mathcal{O}(\alpha_s \alpha^8)$ corrections to $q\bar{q}$ are α-suppressed, as expected: they amount to roughly a per-mille of the corresponding NLO_1 term. The NLO_3 QCD corrections to the $\gamma\gamma$-induced process are fully negligible. In the γg partonic channel, the NLO_3 corrections are of purely EW nature and amount to 7% of the QCD corrections of order NLO_2. An even stronger suppression is visible in the γb channels, which enter this order as real EW corrections to the LO interference.

perturbative order	σ_{nob} [ab]	$\frac{\sigma_{\text{nob}}}{\sigma_{\text{nob, LO}_1}}$	σ_{b} [ab]	$\frac{\sigma_{\text{b}}}{\sigma_{\text{nob, LO}_1}}$	σ [ab]	$\frac{\sigma}{\sigma_{\text{LO}_1}}$
LO$_1$	$107.246(5)^{+35.0\%}_{-24.0\%}$	1.0000	$0.31378(9)$	$+0.0029$	$107.560(5)^{+34.9\%}_{-23.9\%}$	1.0000
LO$_2$	$0.7522(2)^{+11.1\%}_{-9.0\%}$	$+0.0070$	$-0.6305(2)$	-0.0059	$0.1217(3)$	$+0.0011$
LO$_3$	$0.2862(1)^{+3.4\%}_{-3.4\%}$	$+0.0027$	$0.7879(2)$	$+0.0073$	$1.0742(3)^{+12.1\%}_{-14.9\%}$	$+0.0100$
NLO$_1$	$-11.4(1)$	-0.1072	$0.518(3)$	$+0.0048$	$-10.9(1)$	-0.1016
NLO$_2$	$-0.89(1)$	-0.0083	$0.109(3)$	$+0.0010$	$-0.78(1)$	-0.0072
NLO$_3$	$1.126(4)$	$+0.0105$	$-0.089(4)$	-0.0008	$1.037(6)$	$+0.0096$
NLO$_4$	$-0.0340(9)$	-0.0003	$-0.0180(9)$	-0.0002	$-0.052(1)$	-0.0005
LO$_1$+NLO$_1$	$95.8(1)^{+0.4\%}_{-11.2\%}$	$+0.8933$	$0.832(3)$	$+0.0078$	$96.6(1)^{+0.4\%}_{-10.7\%}$	$+0.8984$
LO	$108.285(5)^{+34.7\%}_{-23.8\%}$	$+1.0097$	$0.4713(3)$	$+0.0044$	$108.756(5)^{+34.5\%}_{-23.7\%}$	$+1.0111$
LO+NLO	$97.0(1)^{+0.5\%}_{-11.2\%}$	$+0.9052$	$0.991(6)$	$+0.0092$	$98.0(1)^{+0.4\%}_{-10.6\%}$	$+0.9114$

Table 3. LO cross-sections and NLO corrections (in ab) in the fiducial setup. In the second column all partonic channels are included in σ_{nob} except the ones having at least one bottom quark in the initial state, while σ_{b} includes all these channels. The sum of the two (σ) is shown in the sixth column. Ratios with respect to the cross-section σ_{nob} at LO$_1$ accuracy are reported in the third and fifth column. In the seventh column ratios are shown with respect to the full LO$_1$ cross-section including the bottom channels, as well. Integration errors are given in parentheses and percentage 7-point scale variations as super- and sub-scripts.

All NLO$_4$ corrections for each partonic channel are consistently found to be α-suppressed with respect to the corresponding LO$_3$ and overall negligible compared to the other corrections. This last statement holds true for all channels receiving an $\mathcal{O}(\alpha^9)$ contribution, with the exception of the bb/$\bar{\text{b}}\bar{\text{b}}$ bottom ones (whose NLO$_1$ corrections were already 3×10^{-4} ab) and the $q\bar{q}$ ones, with a negative NLO$_4$ term of the same order of magnitude as the NLO$_3$ one. The overall NLO$_4$ result is dominated by the negative contribution of $q\bar{q}$/b$\bar{\text{b}}$ channels, with a positive γq/γb contribution roughly giving a 10% of the former. The EW corrections to the di-photon channel, whose virtual contribution has been the most CPU-expensive part of the calculation to evaluate, is the smallest correction amongst the ones in table 2 (less than half of the QCD corrections to this channel) and therefore fully negligible.

Results for the integrated cross-sections, which have been separately shown for the different partonic channels in tables 1 and 2, are collected in table 3. Theoretical uncertainties in the results are estimated with 7-point scale variations, as described in section 3.1. We refrain from showing scale uncertainties for LO$_2$ results in all cases where interference contributions from bottom-induced diagrams are present. For such contributions, the QCD-scale (renormalisation- and factorisation-scale) uncertainties do not have a clear interpretation. However, the scale uncertainties are shown for the LO$_2$ contribution from the γg process. Uncertainty bands for LO$_3$ results come uniquely from factorisation-scale variations, owing to the EW nature of the contribution, which is also why they turn out to be smaller than the LO$_1$ ones.

In the second column of table 3 we present results for the integrated cross-section σ_{nob} at different perturbative accuracies: all partonic channels are included, except the ones involving at least one bottom quark in the initial state. The contribution σ_{b} to the integrated cross-section, namely the sum of all bottom-induced contributions, is presented in the fourth column individually for each perturbative order. The results accounting for all partonic channels ($\sigma = \sigma_{\mathrm{nob}} + \sigma_{\mathrm{b}}$) are reported in the sixth column of the table. For the bottom contributions alone, we also decided not to report scale uncertainties: since the running of the bottom PDFs that enters when computing the scale envelope includes also contributions from other quark flavours, the interpretation of the scale-uncertainty bands for these comparably small contributions is unclear and not particularly revealing. The scale variations for bottom-induced contributions are instead properly taken into account for the complete result σ.

From table 3, one can notice that the LO contribution to σ_{nob} is dominated by the LO_1 term. The largest NLO correction is represented by the NLO_1 term: with our scale choice of eq. (3.10) it roughly amounts to a -10% correction of the LO_1 result and its inclusion significantly reduces the size of QCD-scale uncertainties. The NLO_3 turns out to be the largest NLO contribution amongst the subleading ones, providing a positive 1% correction to LO_1. Since LO_3 is a purely EW contribution, no improvement in QCD-scale uncertainty is obtained when adding the NLO_3 correction. The NLO_2 term is slightly smaller than the NLO_3 one, but being negative, largely cancels the effect of the NLO_3 contribution, so that the sum $\mathrm{NLO}_2 + \mathrm{NLO}_3$ only corrects the LO_1 by 0.2%. Finally, the NLO_4 just affects the NLO result for σ_{nob} at the sub-per-mille level. Due to their EW nature (with the exception of the small contribution arising from the QCD corrections to LO_2) both NLO_2 and NLO_4 do not further reduce the scale uncertainties.

The $\mathrm{LO}_{\mathrm{b},1}$ contribution for the bottom channel is comparable in size to the subleading $\mathrm{LO}_{\mathrm{b},2}$ and $\mathrm{LO}_{\mathrm{b},3}$ terms. The sum of these three LO perturbative orders only modifies the complete LO result for σ at the per-mille level, also as a consequence of large cancellations occurring amongst them. A similar impact on the full NLO result for σ is observed for the set of NLO corrections in bottom-induced channels. The largest contribution still arises from the $\mathrm{NLO}_{\mathrm{b},1}$ perturbative order, which changes the NLO_1 corrections computed without including the bottom contributions by -4%. The $\mathrm{NLO}_{\mathrm{b},2}$ and $\mathrm{NLO}_{\mathrm{b},3}$ corrections are again comparable in size but, due to their opposite signs, compensate each other to a large extent. The NLO_4 corrections to σ, 35% of which comes from the bottom-induced channels, still remain negligible compared to the other NLO terms. Therefore, the LO+NLO result for σ only receives roughly a $+1\%$ correction after including the bottom channels at all LO and NLO perturbative orders.

As a general remark, we stress that the cancellations of contributions between different partonic channels should not be viewed as a general feature but might be related to our specific event selection. The sizes of the individual channels are more characteristic than sums of different contributions.

3.3 Differential cross-sections

In this section we study the impact of including the NLO corrections at differential level, by examining some relevant distributions. Since NLO_4 corrections have already been shown in

the previous section to be fully negligible and out of reach in any foreseen LHC experimental measurement, we refrain from including them in our differential results. Unless otherwise stated, all predictions include bottom-initiated contributions. Whenever presented, the uncertainty bands are obtained by means of 7-point scale variations performed at the bin-by-bin level.

All plots are characterised by the following structure. In a main panel the three LO contributions are presented with dashed lines, namely the LO_1 (blue curve), the LO_2 (magenta curve) and LO_3 (turquoise curve). The last two contributions are shown after scaling them up by a factor of 10. In the same panel, the genuine NLO QCD result, obtained by correcting the LO_1 result by NLO_1, is shown in red, together with the full NLO prediction LO+NLO, shown in brown. All plots are supplemented with at least two ratio panels. The first one shows again the LO_3 curve but also the three NLO corrections, namely NLO_1 (in red), NLO_2 (in green), and NLO_3 (in goldenrod), normalised to the LO_1 result. Since the LO_2 contribution is typically negligible or at most similar in size to the LO_3 one, we refrain from including its curve in any ratio panel, with just one exception for the distribution in the invariant mass of the τ-lepton pair (as justified below). A second ratio panel compares the $LO_1 + NLO_1$ result with the complete LO+NLO prediction, both normalised with respect to the former. For a selected set of distributions two additional ratio panels are included. The first additional panel reports three curves, normalised to the LO_1 result: the NLO_2 and NLO_3 corrections are included again as a reference together with an additional purple curve, which includes photon-induced channels (namely all channels having at least one photon as an initial-state parton). The second additional panel is added to illustrate the impact of the bottom-induced contributions. Our full LO+NLO prediction is reported together with the $(LO + NLO)_{nob}$ result (dash-dotted orange curve), where all channels with at least one initial-state bottom have been excluded: the latter prediction is also used for normalisation.

We consider observables that are directly measurable at the LHC as well as observables that rely on Monte Carlo truth. The latter refer to kinematic variables of the top and antitop quark or of jets initiated by bottom/antibottom quarks arising from the top/antitop decays. As already mentioned, some partonic channels may include up to three final-state bottom quarks. Moreover, since our jet-clustering algorithm does not distinguish bottom and antibottom, bottom jets are identified as originating from a top or antitop quark by maximising the likelihood function $\mathcal{L}$, defined as a product of two Breit-Wigner distributions corresponding to the top-quark and antitop-quark propagators,

$$\mathcal{L}(p_{b_i}, p_{b_j}) = \frac{1}{\left(p_{e^+\nu_e b_i}^2 - m_t^2\right)^2 + (m_t\Gamma_t)^2} \frac{1}{\left(p_{\mu^-\bar{\nu}_\mu b_j}^2 - m_t^2\right)^2 + (m_t\Gamma_t)^2}, \qquad (3.13)$$

where the momenta p_{abc} are defined as $p_{abc} = p_a + p_b + p_c$. Notice that at the Monte Carlo-truth level the neutrino flavour is accessible. The combination of momenta $\{p_{b_i}, p_{b_j}\}$ (at most nine for channels with three final-state bottom quarks) that maximises this function defines the two bottom jets originating from top quarks: the first momentum of the pair is identified with a bottom quark and the second with an antibottom quark. The top- and
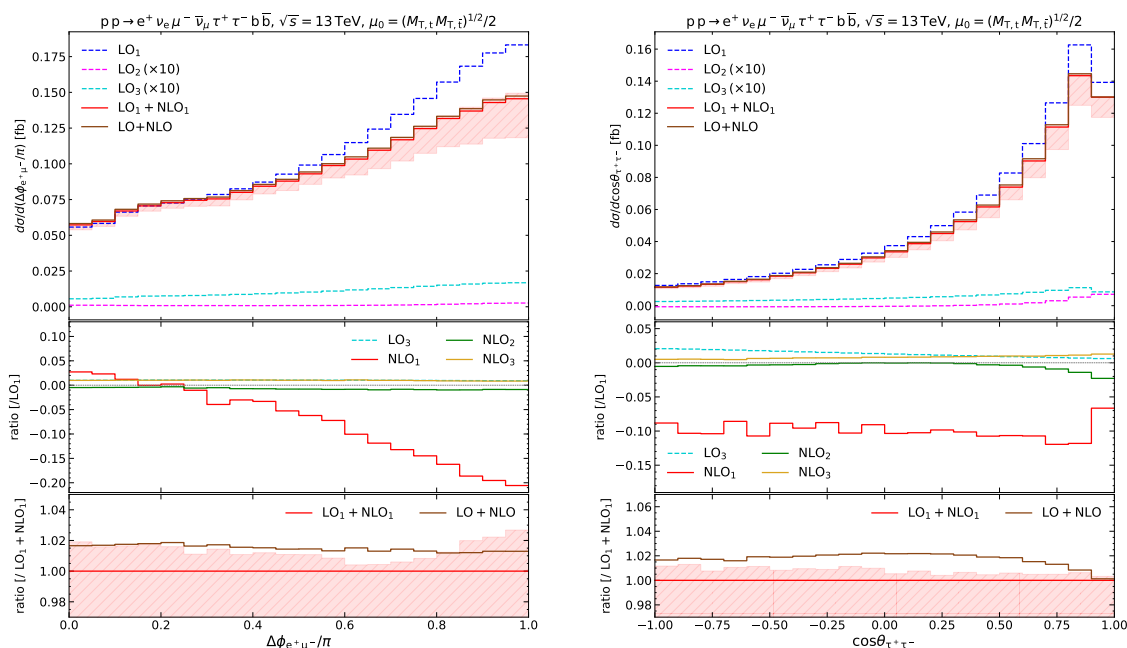
(a) Azimuthal-angle separation between the positron and the muon in units of π.

(b) Cosine of the angle between τ^+ and τ^-.

Figure 12. Distributions in the azimuthal-angle separation between the positron and the muon in units of π (left) and in the cosine of the angle between the two τ leptons (right). The different NLO corrections for the observables are compared separately (first ratio panels) and at the level of the full prediction (second ratio panel).

antitop-quark momenta are then computed as

$$p_{\mathrm{t}} = p_{\mathrm{e^+}\nu_{\mathrm{e}}\mathrm{b}_i} \qquad \text{and} \qquad p_{\bar{\mathrm{t}}} = p_{\mu^- \bar{\nu}_\mu \mathrm{b}_j} \,, \tag{3.14}$$

respectively. Owing to the final state involving three different lepton flavours, all considered observables refer to charged leptons via their flavours with no need to introduce a transverse-momentum ordering. In the dominant $\mathrm{t\bar{t}}$-resonant topologies, the $\tau^+\tau^-$ pair is unambiguously associated to a potential Z/γ^* boson. All leptons are understood as dressed leptons (see section 3.1).

We start the discussion by examining the two angular distributions in figure 12. In figure 12(a) the distribution in the azimuthal-angle separation between the positron and the muon $\Delta\phi_{\mathrm{e^+}\mu^-}$ is shown. This observable is particularly relevant to constrain some BSM theories and to study the spin correlations of top-antitop pairs. The cross-section shows a minimum at small azimuthal separation and monotonically increases towards larger values of $\Delta\phi_{\mathrm{e^+}\mu^-}$. This trend, which is particularly pronounced at LO_1, is partially mitigated by adding NLO_1 corrections. Indeed, the NLO_1 corrections are positive at $\Delta\phi_{\mathrm{e^+}\mu^-} \approx 0$, where they amount to 2–3%, while they become negative towards large azimuthal separation, reaching more than -20% at $\Delta\phi_{\mathrm{e^+}\mu^-} \approx \pi$. The other contributions, i.e. LO_2, LO_3, NLO_2, and NLO_3, are flat and basically reproduce the relative corrections to the fiducial cross-

section. Adding them to the dominant QCD ones (LO_1 and NLO_1) amounts to a shift in normalisation of about $+1\%$, giving a combined LO+NLO curve sitting at the edge of the scale uncertainty band of the $LO_1 + NLO_1$ result for our scale choice (3.10).

In figure 12(b) the distribution in the cosine of the angle between the two τ leptons is presented. It shows a minimum for $\theta_{\tau^+\tau^-} = \pi$, where the two leptons are produced in a back-to-back configuration. Then, the cross-section steeply increases reaching a maximum around $\cos\theta_{\tau^+\tau^-} \approx 0.85$, where the two leptons are almost collinear. The right-most bin is lower than the previous one, owing to the ΔR distance cut of 0.4 between charged leptons [see eq. (3.7)]. NLO_1 corrections essentially amount to a negative shift in the normalisation of the distribution varying from -9% to -11% throughout the allowed kinematic range, reaching -7% in collinear configurations. The LO_2 contribution weakly increases towards the collinear region until the very last bin of the distribution. The LO_3 contribution reflects the peaked behaviour of the LO_1 term, even though its size is much smaller: it ranges from 2% to about 0.5% of the LO_1 when moving from the anticollinear to the collinear region. The impact of subleading NLO corrections on this observable is quite moderate. NLO_2 corrections are negative and amount to roughly -0.5% in the anticollinear region, almost vanishing in the central emission range of $-0.25 < \cos\theta_{\tau^+\tau^-} < 0.25$ and then decreasing again to -2% in the collinear-emission region. On the other hand, NLO_3 corrections are positive and grow moderately from 0.5% to 1% at $\theta_{\tau^+\tau^-} = 0$. Due to the partial compensation of the different subleading corrections, their overall effect on the normalisation of the $LO_1 + NLO_1$ result vanishes in the collinear region, while it provides a 2% correction in the anticollinear and especially central-emission region, mainly due to the LO_3 and NLO_3 terms.

We turn to the distributions in the rapidity of the muon and of the antitop quark in figures 13(a) and 13(b), respectively. Similar considerations hold for both observables, since the two quantities are largely correlated (in the dominant doubly-resonant topologies the muon is a decay product of the antitop quark). This allows to consider to a good approximation the muon rapidity as a proxy for the antitop one, which cannot be directly measured at the LHC. Both the muon and the antitop quark are preferably produced at central rapidity. The muon-rapidity distribution is cut at $|y_{\mu^-}| < 2.5$ [see eq. (3.7)], while the antitop one is highly suppressed by the rapidity cuts applied on its visible decay products. NLO_1 corrections are negative and roughly -10% throughout the rapidity range, just slowly decreasing in absolute value towards the edges of the distribution (especially for the antitop case, where they amount to -5% around $|y_{\bar{t}}| \approx 2.4$). The LO_3 term mimics the shape behaviour of the LO_1 one to a large extent, even though it represents a small fraction of it (just a 1%). This behaviour was observed for all distributions that we analysed in phase-space regions dominated by on-shell top quarks. The even smaller LO_2 term exhibits a dip at central rapidity: this is due to the fact that the LO_2 result is the sum of a γg contribution, which shows the expected behaviour at central rapidity, and bottom-induced interference terms, which are negative and entirely cancel in our setup the enhancement at zero rapidity of the former contribution. These large cancellations between the two channels at differential level are already manifest for the fiducial cross-sections, as visible in the third column of table 1. Subleading NLO corrections range between -2% and $+1\%$ of the LO_1

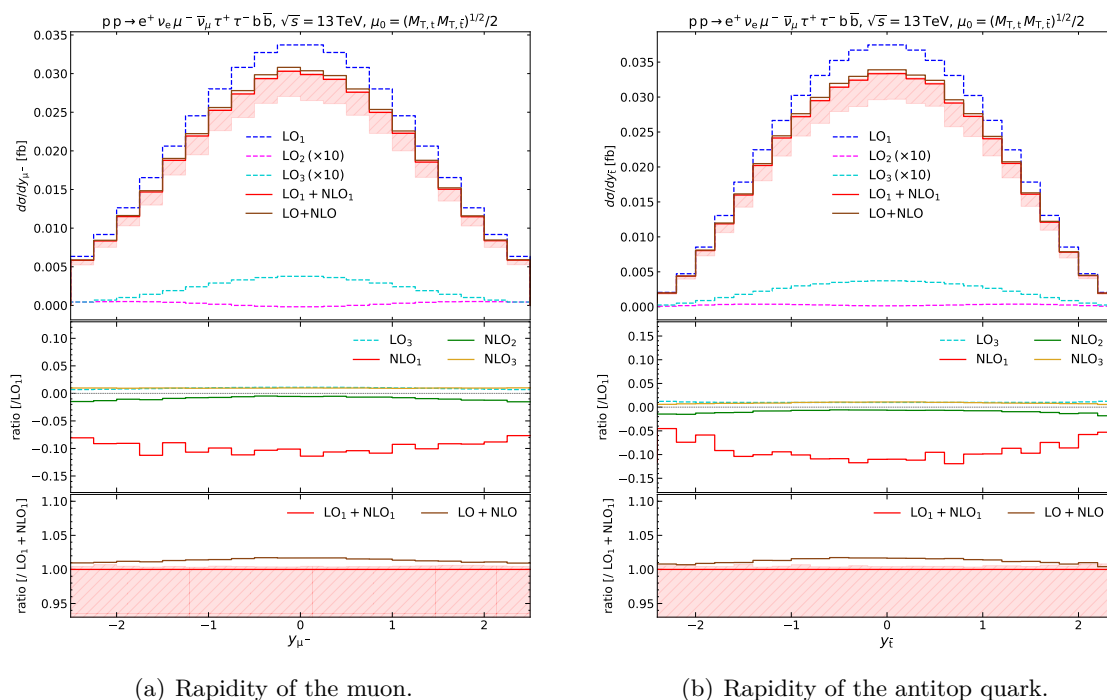(a) Rapidity of the muon.

(b) Rapidity of the antitop quark.

Figure 13. Distributions in the rapidity of the muon (left) and of the antitop quark (right). The different NLO corrections for the observables are compared separately (first ratio panels) and at the level of the full prediction (second ratio panel).

result. Owing to the opposite sign of the NLO_2 and NLO_3 corrections, their overall impact on the combined NLO results is moderate, giving a $+1\%$ normalisation factor (reaching a 4% for the antitop quark in very suppressed forward regions).

We move on presenting some transverse-momentum distributions, which are known to be quite sensitive to EW corrections. In figures 14(a) and 14(b) we display the distributions in the transverse momentum of the $\tau^+\tau^-$ pair and the antitop quark, the latter being accessible only with Monte Carlo truth. In both cases the maximum of the cross-section is around $100\,\mathrm{GeV}$. The NLO_1 corrections are negatively increasing in the most populated region, reaching -15% around $300\,\mathrm{GeV}$, then they decrease and turn positive at very high transverse momenta (as visible for the transverse momentum of the $\tau^+\tau^-$ pair). While the position of the distribution maximum is unchanged when computing the LO_3 contributions, for LO_2 it is shifted to higher values as a result of the negative interference contribution in bottom-induced channels at low transverse momentum. Indeed, in this region the bottom-interference terms are as large as the γg ones but of opposite sign. On the other hand, towards the tails of the distribution the LO_2 result is dominated by the positive γg cross-section, which even exceeds the LO_3 one for $p_{\mathrm{T},t\bar{t}}$. A similar behaviour of the LO_2 terms was found in all transverse-momentum distributions that we have studied, i.e. large cancellations for small transverse momenta but dominance of photon-induced contributions at larger p_{T}. Moving to NLO subleading corrections, NLO_2 are by far the dominant ones for these observables. The correction with respect to the LO_1 result is positive at low transverse

(a) Transverse momentum of the $\tau^+\tau^-$ pair.
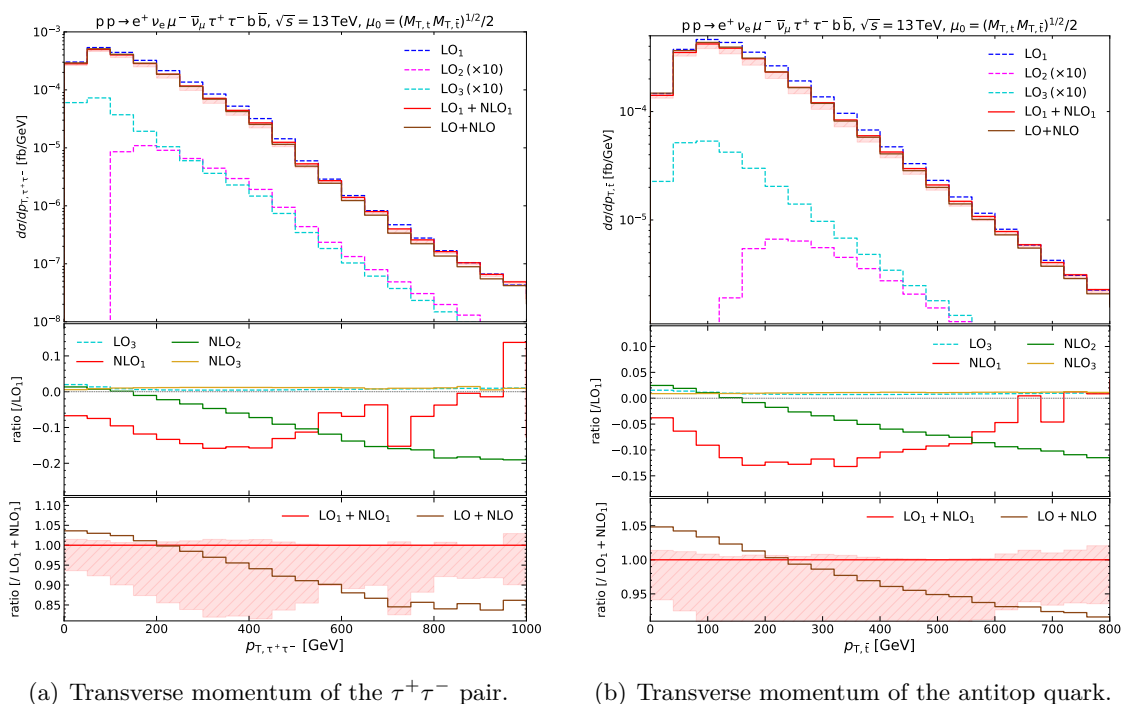
(b) Transverse momentum of the antitop quark.

Figure 14. Distributions in the transverse momentum of the $\tau^+\tau^-$ pair (left) and the antitop quark (right). The different NLO corrections for the observables are compared separately (first ratio panels) and at the level of the full prediction (second ratio panel).

momentum, but constantly decreases showing the expected negative enhancement at high transverse momentum due to the effect of EW Sudakov logarithms [72]: for the $\tau^+\tau^-$ pair the corrections reach -20% at $p_{\mathrm{T},\tau^+\tau^-} = 1\,\mathrm{TeV}$, while for the antitop distribution we observe a -12% at $p_{\mathrm{T},\bar{\mathrm{t}}} = 800\,\mathrm{GeV}$. NLO$_3$ terms only marginally correct the LO$_1$ result: the corrections are roughly 1% for both $p_{\mathrm{T},\tau^+\tau^-}$ and $p_{\mathrm{T},\bar{\mathrm{t}}}$ and essentially constant over the whole range. Clearly, the LO$_1$ + NLO$_1$ distributions are strongly distorted by the inclusion of subleading contributions, with a dominant effect given by NLO$_2$ corrections. Both distributions exhibit a positive correction of 4–5% in the bulk region, which slowly decreases becoming negative around 250 GeV.

In figure 15 two more transverse variables are reported. In figure 15(a) we present our results for the distribution in the transverse momentum of the $\mathrm{b}\bar{\mathrm{b}}$ pair defined at the Monte Carlo-truth level as described at the beginning of this section and in eq. (3.13). As for the transverse momentum of the $\mathrm{t}\bar{\mathrm{t}}$ pair (not shown here), the transverse momentum of the $\mathrm{b}\bar{\mathrm{b}}$ pair is particularly sensitive to QCD corrections to LO$_1$. The QCD corrections are negative and roughly -15% in the bulk of the distribution, then, after changing sign around 200 GeV, they steeply increase up to $+100\%$ at $p_{\mathrm{T},\mathrm{b}\bar{\mathrm{b}}} \approx 600\,\mathrm{GeV}$. These huge effects are not simply explained by the presence of hard QCD real radiation, but are known as giant QCD K-factor [73]. Indeed, at NLO$_1$ topologies of a $\mathrm{t}\bar{\mathrm{t}}\mathrm{j}$ event open up where the emission of a soft and/or collinear Z boson causes the double-logarithmic enhancement of the cross-section in the high transverse-momentum regions of the jet. A similar effect was found also in $\mathrm{t}\bar{\mathrm{t}}\mathrm{W}^{\pm}$

(a) Transverse momentum of the bottom-jet pair.
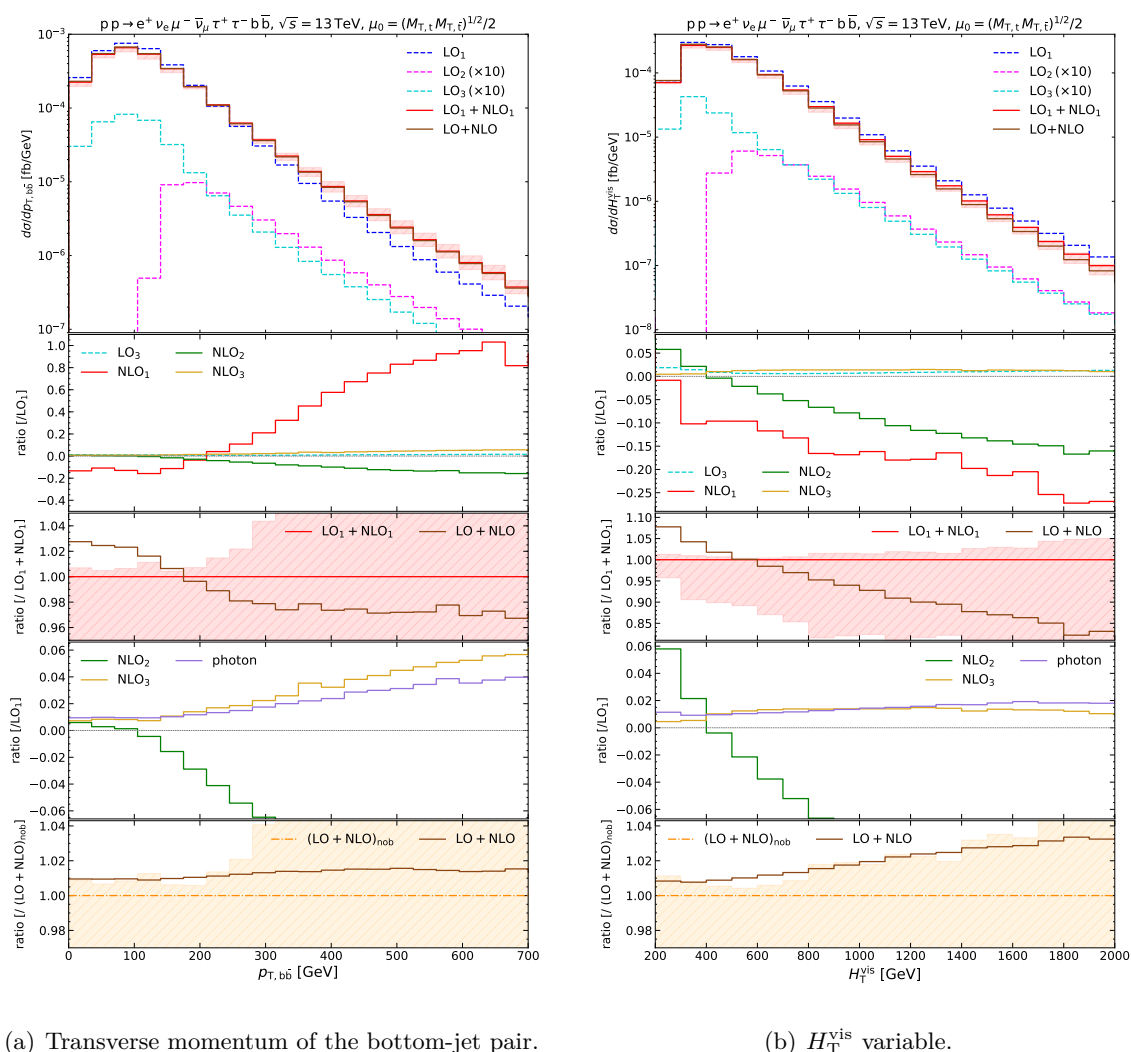
(b) H_T^{vis} variable.

Figure 15. Distributions in the transverse momentum of the bottom-jet pair (left) and in the H_T^{vis} variable (right). The different NLO corrections for the observables are compared separately (first ratio panels) and at the level of the full prediction (second ratio panel). The size of photon-induced channels and bottom contributions are presented in the third and fourth ratio panels, respectively.

production [40]. As a consequence of the very large QCD corrections for large $p_{T,b\bar{b}}$, the scale dependence of the full NLO QCD result is LO like in these regions of phase space. The NLO$_2$ corrections are once again dominated by large and negative EW Sudakov logarithms. They start from small positive values of roughly 0.5% (as visible in the third ratio panel) to reach −15% at $p_{T,b\bar{b}} = 700$ GeV. An opposite behaviour is found for NLO$_3$ corrections, which are ruled by real gluon-induced contributions: being positive and reaching +5% at high transverse momenta, they partially balance the effect of NLO$_2$ corrections in the high-energy tails. Indeed, when considering all subleading contributions, the impact of EW Sudakov logarithms is reduced, and subleading corrections never exceed −3.5%. In the

soft region of the spectrum, i.e. for $p_{\mathrm{T,b\bar{b}}} < 250\,\mathrm{GeV}$, subleading corrections reach at most $+3\%$ of the NLO QCD cross-section. Transverse-momentum distributions are known to be more sensitive to the effects of photon-induced contributions in the tails. In the third ratio panel we show these contributions at NLO accuracy. All partonic channels involving at least one initial-state photon and their NLO corrections are included. For the process at hand, photon-induced contributions receive both $\mathrm{NLO_2}$ and $\mathrm{NLO_3}$ corrections, the latter being essentially EW corrections to the $\gamma\mathrm{g}$ $\mathrm{LO_2}$ term (QCD corrections to the $\gamma\gamma$ channel are fully negligible). In agreement with similar studies for other processes (see for instance ref. [43]), photon contributions slowly increase reaching 4% of the $\mathrm{LO_1}$ contribution at high p_{T} values. This behaviour is explained by the fact that the photon PDF grows faster than the quark and gluon ones in this phase-space region [74]. Finally, in a fourth ratio panel we present the impact of the bottom-induced channels together with their NLO corrections. As already observed in ref. [53], the observables which are expected to be more affected by bottom contributions are the hadronic ones whose definition requires at least one b jet. We see that the inclusion of leading and subleading bottom corrections has a moderate impact on the result, which is corrected by roughly $+1\%$ in the bulk of the distribution and up to $+1.5\%$ in the tails. Nevertheless, these corrections are entirely covered by the theory uncertainty bands of the NLO result not including the bottom channels.

In figure 15(b) we present another variable of interest for LHC searches, namely $H_{\mathrm{T}}^{\mathrm{vis}}$, defined as

$$H_{\mathrm{T}}^{\mathrm{vis}} = p_{\mathrm{T,b_1}} + p_{\mathrm{T,b_2}} + p_{\mathrm{T},\tau^+} + p_{\mathrm{T},\tau^-} + p_{\mathrm{T},\mu^-} + p_{\mathrm{T},e^+}\,, \tag{3.15}$$

similarly to H_{T} in eq. (3.9) but without including the missing-energy contribution. Since in our calculation up to three b jets can be produced, the sum of the transverse momenta is restricted to the leading and subleading b jets (here $\mathrm{b_1}$ and $\mathrm{b_2}$, respectively) defined according to a p_{T} ordering. We see that also for this observable $\mathrm{NLO_1}$ QCD corrections are large, reaching more than -25% at $2\,\mathrm{TeV}$. $\mathrm{NLO_2}$ corrections amount to 6% at low $H_{\mathrm{T}}^{\mathrm{vis}}$ values, steadily decreasing and becoming negative towards higher values. The impact of EW Sudakov logarithms is less pronounced than in the $p_{\mathrm{T,b\bar{b}}}$ distribution, with a correction relative to $\mathrm{LO_1}$ of around -15% at $2\,\mathrm{TeV}$. The $\mathrm{NLO_3}$ contributions account for at most $+1\%$ and are essentially flat up to very high $H_{\mathrm{T}}^{\mathrm{vis}}$ values. Overall, the subleading NLO corrections are dominated by the $\mathrm{NLO_2}$ corrections in the high-energy regime. The impact of photon-induced contributions is slightly milder than for $p_{\mathrm{T,b\bar{b}}}$, amounting to roughly 1% of $\mathrm{LO_1}$ at low $H_{\mathrm{T}}^{\mathrm{vis}}$ values and increasing to almost a 2% towards the tail. Since b jets are involved in the definition of the observable in eq. (3.15), we might expect that bottom-induced channels play a role. Indeed, in the fourth ratio panel in figure 15(b) some shape effects are found, owing to the inclusion of the bottom contributions, which correct the σ_{nob} result from $+1\%$ in the very first bin up to $+3.5\%$ at $H_{\mathrm{T}}^{\mathrm{vis}} = 2\,\mathrm{TeV}$.

In figure 16 we consider two invariant-mass variables. We start with the distribution in the invariant mass of the antitop quark displayed in figure 16(a). The characteristic invariant-mass peak at $m_{\mathrm{t}} = 173\,\mathrm{GeV}$ is found in the $\mathrm{LO_1}$ and in the $\mathrm{LO_3}$ results. Conversely, the $\mathrm{LO_2}$ shows a dip in that region, as a consequence of the negative bottom-interference contributions, which overcompensate the resonance peak of the $\mathrm{LO_2}$ $\gamma\mathrm{g}$ term leading to a
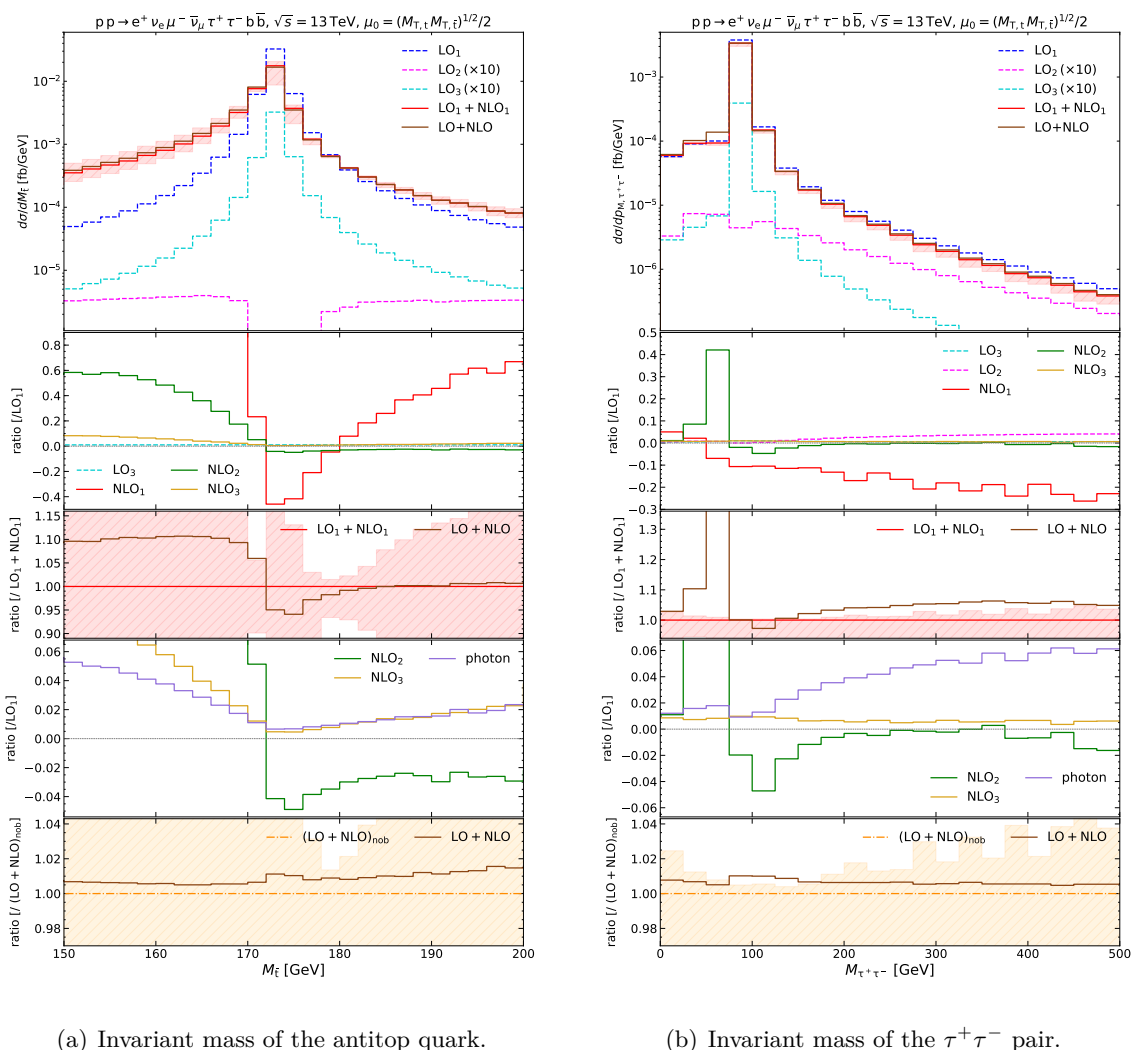
(a) Invariant mass of the antitop quark.

(b) Invariant mass of the $\tau^+\tau^-$ pair.

Figure 16. Distributions in the invariant mass of the antitop quark (left) and of the $\tau^+\tau^-$ pair (right). The different NLO corrections for the observables are compared separately (first ratio panels) and at the level of the full prediction (second ratio panel). The size of photon-induced channels and bottom contributions are presented in the third and fourth ratio panels, respectively.

slightly negative LO_2 contribution near the nominal top mass. Our results for the NLO_1 corrections are in line with the results for this observable found in $t\bar{t}$ [75] and $t\bar{t}W^\pm$ [40] production. The QCD corrections are negative (around -40%) on the peak, while they become positive in regions where the antitop quark is off shell: for regions of a reconstructed antitop mass above the peak, i.e. $M_{\bar{t}} > m_t$, the corrections progressively increase reaching up to $+60\%$ for $M_{\bar{t}} \approx m_t + 25\,\mathrm{GeV}$; for $M_{\bar{t}} < m_t$ the $LO_1 + NLO_1$ result is one order of magnitude larger than its LO_1 one. The enhancement below the peak is well-known and due to QCD radiation that is not clustered with the b jet arising from the antitop-quark decay. Radiative-tail effects are also present in subleading NLO corrections, even though

to a lesser extent. Indeed, in $\mathrm{NLO_2}$ corrections real-photon radiation can also be emitted from the muon arising from the antitop quark. Owing to the suppression of the EW versus the QCD coupling, this gives rise to smaller corrections with respect to $\mathrm{LO_1}$, reaching $+60\%$ for $M_{\bar{\mathrm{t}}} \approx m_{\mathrm{t}} - 20\,\mathrm{GeV}$. The $\mathrm{NLO_2}$ corrections are negative at the peak (around -4%) as well as in the off-shell region above the pole mass. Yet another behaviour is found for the $\mathrm{NLO_3}$ contribution, which remains positive throughout the considered spectrum. It reaches a minimum of 0.5% around the top resonance, while increasing in the off-shell regions: for $M_{\bar{\mathrm{t}}} \approx m_{\mathrm{t}} + 25\,\mathrm{GeV}$ a 2% correction is found, and for $M_{\bar{\mathrm{t}}} \approx m_{\mathrm{t}} - 20\,\mathrm{GeV}$ the radiative tail generates a 10% correction. The behaviour of $\mathrm{NLO_3}$ corrections is dominated by quark-gluon partonic channels, which involve a quark in the final state that cannot arise from the radiative decay of the top or the antitop quark, differently from a final-state gluon or photon (as observed in ref. [41]). The complete set of subleading corrections to the NLO QCD result just reinforces the behaviour of the QCD corrections: it amounts to an essentially constant $+10\%$ effect below the peak, to a negative correction of roughly -5% around $M_{\bar{\mathrm{t}}} \approx m_{\mathrm{t}}$, and is almost vanishing for $M_{\bar{\mathrm{t}}} > m_{\mathrm{t}}$. As already observed for $\mathrm{t\bar{t}}$ production [43], the role of photon-initiated contributions in invariant-mass distributions can be quite significant. In our case we see that the full set of photon-induced channels mimics the $\mathrm{NLO_3}$ behaviour, being always positive and growing towards the off-shell regions. The radiative-tail enhancement mostly comes from the $\gamma\mathrm{g}$ channel, reaching $+5.5\%$ at $M_{\bar{\mathrm{t}}} \approx m_{\mathrm{t}} - 20\,\mathrm{GeV}$. Since the definition of this variable involves just one bottom quark for the reconstruction of the antitop-quark mass at Monte Carlo-truth level, the role of the bottom contributions is slightly smaller than for other distributions analysed previously. They essentially give a contribution to the combined NLO cross-section ranging from 0.5% to 1.5%.

In figure 16(b) we present the distribution in the invariant mass of the $\tau^+\tau^-$ pair. The peak at the Z-boson mass is observed for $\mathrm{LO_1}$ and $\mathrm{LO_3}$, but appears to be completely absent for $\mathrm{LO_2}$. In fact there is even a slight dip in the bin containing the Z-boson mass. As discussed for figure 16(a), this results once again from large cancellations between the $\gamma\mathrm{g}$ and the bottom-induced interference terms in the resonant region. The harder tail of the $\mathrm{LO_2}$ curve as compared to $\mathrm{LO_3}$ is instead entirely due to the $\gamma\mathrm{g}$ channel, which is by far the largest subleading contribution in the tail, accounting for a $+4\%$ correction with respect to $\mathrm{LO_1}$. The $\mathrm{NLO_1}$ corrections constantly decrease from $+4\%$ in the very first bin of the distribution to roughly -20% in the far off-shell region. Since the observable at hand is fully leptonic, large radiative effects are generated by $\mathrm{NLO_2}$ corrections, owing to real photons that are not clustered with τ leptons: the $\mathrm{NLO_2}$ corrections with respect to $\mathrm{LO_1}$ are indeed more than $+40\%$ right below the peak and -2% for $M_{\tau^+\tau^-} \approx M_{\mathrm{Z}}$. Above this region they increase, almost vanish around $300\,\mathrm{GeV}$, and then mildly decrease again. Since the $\mathrm{NLO_3}$ contributions are effectively dominated by QCD corrections, they do not affect the position of the resonance peak, like $\mathrm{NLO_1}$, but they provide an essentially constant correction to the $\mathrm{LO_1}$ cross-section ranging from $+0.5\%$ to $+1\%$. Therefore, subleading contributions to $M_{\tau^+\tau^-}$ mainly arise from $\mathrm{LO_2}$ contributions in the region $M_{\tau^+\tau^-} \gtrsim 150\,\mathrm{GeV}$, while the $\mathrm{NLO_2}$ corrections dominate around and below the Z-boson mass. The photon-induced contributions are quite relevant, increasing from roughly 1% at $M_{\tau^+\tau^-} \approx M_{\mathrm{Z}}$ up to 6%

at $500\,\mathrm{GeV}$, due to the leptonic nature of the observable. The impact of bottom-initiated contributions is instead negligible: they only mildly distort the shape of the distribution by a positive correction of at most 1%, which is entirely contained within the theory uncertainty of the result without bottom contributions.

4   Conclusions

We have presented the first calculation of the off-shell production of a top-antitop pair in association with a Z boson that is accurate both at NLO QCD and NLO EW for $13\,\mathrm{TeV}$ proton-proton collisions. To be more precise, we have computed the entire tower of LO contributions and NLO corrections to a final state that involves four different charged leptons, two bottom jets, and missing transverse momentum. All off-shell effects have been retained in order to provide a realistic description of the process including decay effects at NLO accuracy.

Owing to the very high multiplicity of the final state, this calculation proved to be extremely intensive from the computation-time and book-keeping point of view. In this sense, the off-shell $t\bar{t}Z$ process lies at the frontier of LHC signatures that can be simulated with optimised Monte Carlo integrators and one-loop amplitude providers that are currently available. Given the high complexity of the simulations, we have performed a careful validation of the QCD corrections with existing results [39], finding very good agreement both in integrated and in differential cross-sections.

Even if bottom-induced partonic processes were already considered in the context of NLO QCD predictions for $t\bar{t}$-associated processes [53], our calculation is the first one that accounts for all LO and NLO contributions to these channels, i.e. we provide predictions in a truly five-flavour scheme. Also photon-induced processes have been taken into account, in spite of the expected minor impact on the final results. Throughout our calculation full spin correlations have been kept, while including both resonant and non-resonant diagrams. The mixing of QCD and EW radiative corrections as well as all interference effects have been taken into account.

We provide integrated and differential results in a realistic fiducial setup, using a resonance-aware definition for the renormalisation and factorisation scales, which is known to improve the convergence of the perturbative expansion in α_s [41]. With such a choice, the QCD corrections to the LO QCD (LO_1) cross-section, namely NLO_1, are sizeable and negative (-10%) at integrated level, and decrease the QCD-scale uncertainties from 30% down to 10% when going from LO_1 to $\mathrm{LO}_1 + \mathrm{NLO}_1$. The NLO_2 corrections (EW corrections to LO QCD and QCD corrections to LO interference) account for less than a percent of the LO fiducial cross section and are comparable in size with the NLO_3 contributions (EW corrections to LO interference and QCD corrections to LO EW), where the expected α suppression is balanced by the enhancement owing to tZ-scattering topologies in the real corrections. On the other hand, our calculation confirms the expectation that NLO_4 corrections (EW corrections to LO EW) are very strongly suppressed, giving a sub-per-mille effect that is definitely out of reach at the LHC even after the planned luminosity upgrades. The contributions of bottom-induced and photon-induced channels are each about 1% of the complete NLO cross-section. In particular, we have observed in our fiducial setup

strong cancellations between the bottom-induced contributions and photon-gluon-induced ones, occurring already at the integrated level for the LO_2 cross-section. This interplay amongst the various LO and NLO corrections gives an even more intricate structure at differential level. All NLO corrections do not just cause a change of normalisation but also a distortion of the distribution shapes, even for some more inclusive observables like angles and rapidities. Remarkable shape changes at NLO_1 are motivated by an overall strong scale dependence, but also by the presence of hard real radiation, which gives LO-like scale bands in tails of some distributions. After including NLO_2 and NLO_3 corrections, the differential cross-sections change sizeably w.r.t. the pure QCD result ($LO_1 + NLO_1$) especially in transverse-momentum distributions, pointing out that the NLO_1, NLO_2, and NLO_3 corrections are unavoidable for a description of the $t\bar{t}Z$ process when aiming at precise predictions over the full phase space. In particular, a sizeable enhancement from EW Sudakov logarithms gives NLO_2 corrections that reach up to -20% of the LO_1 result at moderate-to-high transverse momenta. The differential NLO_3 corrections are usually flatter than the other two. As a general comment, in phase-space regions where the cross-section is sizeable, the subleading NLO corrections are below 5%.

We conclude stressing that, although an on-shell calculation (or one including decay effects via a production×decay approximation) is expected to capture most of the $t\bar{t}Z$ features in the bulk regions of the phase space, it is essential to simulate this process including all kinds of off-shell effects, especially in the case where exclusive fiducial selections are applied and differential measurements are performed.

Acknowledgments

References

[1] A. Buckley et al., *Constraining top quark effective theory in the LHC Run II era*, *JHEP* **04** (2016) 015 [arXiv:1512.03360] [InSPIRE].

[2] O. Bessidskaia Bylund et al., *Probing top quark neutral couplings in the Standard Model Effective Field Theory at NLO in QCD*, *JHEP* **05** (2016) 052 [arXiv:1601.08193] [InSPIRE].

[3] P. Cox, A.D. Medina, T.S. Ray and A. Spray, *Novel collider and dark matter phenomenology of a top-philic Z′*, *JHEP* **06** (2016) 110 [arXiv:1512.00471] [InSPIRE].

[4] J.H. Kim, K. Kong, S.J. Lee and G. Mohlabeng, *Probing TeV scale Top-Philic Resonances with Boosted Top-Tagging at the High Luminosity LHC*, *Phys. Rev. D* **94** (2016) 035023 [arXiv:1604.07421] [InSPIRE].

[5] P.J. Fox, I. Low and Y. Zhang, *Top-philic Z′ forces at the LHC*, *JHEP* **03** (2018) 074 [arXiv:1801.03505] [INSPIRE].

[6] E. Alvarez, A. Juste, M. Szewc and T. Vazquez Schroeder, *Topping-up multilepton plus b-jets anomalies at the LHC with a Z′ boson*, *JHEP* **05** (2021) 125 [arXiv:2011.06514] [INSPIRE].

[7] S. Bißmann, G. Hiller, C. Hormigos-Feliu and D.F. Litim, *Multi-lepton signatures of vector-like leptons with flavor*, *Eur. Phys. J. C* **81** (2021) 101 [arXiv:2011.12964] [INSPIRE].

[8] U. Baur, A. Juste, L.H. Orr and D. Rainwater, *Probing electroweak top quark couplings at hadron colliders*, *Phys. Rev. D* **71** (2005) 054013 [hep-ph/0412021] [INSPIRE].

[9] U. Baur, A. Juste, D. Rainwater and L.H. Orr, *Improved measurement of ttZ couplings at the CERN LHC*, *Phys. Rev. D* **73** (2006) 034016 [hep-ph/0512262] [INSPIRE].

[10] E.L. Berger, Q.-H. Cao and I. Low, *Model Independent Constraints Among the Wtb, Zb anti-b, and Zt anti-t Couplings*, *Phys. Rev. D* **80** (2009) 074020 [arXiv:0907.2191] [INSPIRE].

[11] R. Röntsch and M. Schulze, *Constraining couplings of top quarks to the Z boson in $t\bar{t} + Z$ production at the LHC*, *JHEP* **07** (2014) 091 [*Erratum ibid.* **09** (2015) 132] [arXiv:1404.1005] [INSPIRE].

[12] R. Röntsch and M. Schulze, *Probing top-Z dipole moments at the LHC and ILC*, *JHEP* **08** (2015) 044 [arXiv:1501.05939] [INSPIRE].

[13] F. Maltoni, L. Mantani and K. Mimasu, *Top-quark electroweak interactions at high energy*, *JHEP* **10** (2019) 004 [arXiv:1904.05637] [INSPIRE].

[14] G. Durieux et al., *The electro-weak couplings of the top and bottom quarks — Global fit and future prospects*, *JHEP* **12** (2019) 098 [*Erratum ibid.* **01** (2021) 195] [arXiv:1907.10619] [INSPIRE].

[15] I. Brivio et al., *O new physics, where art thou? A global search in the top sector*, *JHEP* **02** (2020) 131 [arXiv:1910.03606] [INSPIRE].

[16] Y. Afik et al., *Multi-lepton probes of new physics and lepton-universality in top-quark interactions*, *Nucl. Phys. B* **980** (2022) 115849 [arXiv:2111.13711] [INSPIRE].

[17] R. Rahaman, *On two-body and three-body spin correlations in leptonic $t\bar{t}Z$ production and anomalous couplings at the LHC*, *JHEP* **02** (2023) 077 [arXiv:2204.12152] [INSPIRE].

[18] J.A. Dror, M. Farina, E. Salvioni and J. Serra, *Strong tW Scattering at the LHC*, *JHEP* **01** (2016) 071 [arXiv:1511.03674] [INSPIRE].

[19] G. Bevilacqua et al., *Towards constraining Dark Matter at the LHC: Higher order QCD predictions for $t\bar{t} + Z(Z \to \nu_\ell \bar{\nu}_\ell)$*, *JHEP* **11** (2019) 001 [arXiv:1907.09359] [INSPIRE].

[20] ATLAS collaboration, *Measurement of the $t\bar{t}W$ and $t\bar{t}Z$ production cross sections in pp collisions at $\sqrt{s} = 8$ TeV with the ATLAS detector*, *JHEP* **11** (2015) 172 [arXiv:1509.05276] [INSPIRE].

[21] CMS collaboration, *Observation of top quark pairs produced in association with a vector boson in pp collisions at $\sqrt{s} = 8$ TeV*, *JHEP* **01** (2016) 096 [arXiv:1510.01131] [INSPIRE].

[22] ATLAS collaboration, *Measurement of the $t\bar{t}Z$ and $t\bar{t}W$ production cross sections in multilepton final states using $3.2\,fb^{-1}$ of pp collisions at $\sqrt{s} = 13$ TeV with the ATLAS detector*, *Eur. Phys. J. C* **77** (2017) 40 [arXiv:1609.01599] [INSPIRE].

[23] CMS collaboration, *Measurement of the cross section for top quark pair production in association with a W or Z boson in proton-proton collisions at $\sqrt{s} = 13$ TeV*, *JHEP* **08** (2018) 011 [arXiv:1711.02547] [INSPIRE].

[24] ATLAS collaboration, *Measurement of the $t\bar{t}Z$ and $t\bar{t}W$ cross sections in proton-proton collisions at $\sqrt{s} = 13$ TeV with the ATLAS detector*, *Phys. Rev. D* **99** (2019) 072009 [arXiv:1901.03584] [INSPIRE].

[25] CMS collaboration, *Measurement of top quark pair production in association with a Z boson in proton-proton collisions at $\sqrt{s} = 13$ TeV*, *JHEP* **03** (2020) 056 [arXiv:1907.11270] [INSPIRE].

[26] ATLAS collaboration, *Measurements of the inclusive and differential production cross sections of a top-quark-antiquark pair in association with a Z boson at $\sqrt{s} = 13$ TeV with the ATLAS detector*, *Eur. Phys. J. C* **81** (2021) 737 [arXiv:2103.12603] [INSPIRE].

[27] F. Maltoni, D. Pagani and I. Tsinikos, *Associated production of a top-quark pair with vector bosons at NLO in QCD: impact on $t\bar{t}H$ searches at the LHC*, *JHEP* **02** (2016) 113 [arXiv:1507.05640] [INSPIRE].

[28] A. Lazopoulos, T. McElmurry, K. Melnikov and F. Petriello, *Next-to-leading order QCD corrections to $t\bar{t}Z$ production at the LHC*, *Phys. Lett. B* **666** (2008) 62 [arXiv:0804.2220] [INSPIRE].

[29] A. Kardos, Z. Trocsanyi and C. Papadopoulos, *Top quark pair production in association with a Z-boson at NLO accuracy*, *Phys. Rev. D* **85** (2012) 054015 [arXiv:1111.0610] [INSPIRE].

[30] S. Frixione et al., *Electroweak and QCD corrections to top-pair hadroproduction in association with heavy bosons*, *JHEP* **06** (2015) 184 [arXiv:1504.03446] [INSPIRE].

[31] R. Frederix et al., *The automation of next-to-leading order electroweak calculations*, *JHEP* **07** (2018) 185 [*Erratum ibid.* **11** (2021) 085] [arXiv:1804.10017] [INSPIRE].

[32] M.V. Garzelli, A. Kardos, C.G. Papadopoulos and Z. Trocsanyi, *Z^0-boson production in association with a top anti-top pair at NLO accuracy with parton shower effects*, *Phys. Rev. D* **85** (2012) 074022 [arXiv:1111.1444] [INSPIRE].

[33] M.V. Garzelli, A. Kardos, C.G. Papadopoulos and Z. Trocsanyi, *$t\bar{t}W^{\pm}$ and $t\bar{t}Z$ hadroproduction at NLO accuracy in QCD with Parton Shower and Hadronization effects*, *JHEP* **11** (2012) 056 [arXiv:1208.2665] [INSPIRE].

[34] M. Ghezzi et al., *Hadronic production of top-quark pairs in association with a pair of leptons in the powheg box framework*, *Phys. Rev. D* **106** (2022) 014001 [arXiv:2112.08892] [INSPIRE].

[35] A. Broggio et al., *Associated production of a top pair and a Z boson at the LHC to NNLL accuracy*, *JHEP* **04** (2017) 105 [arXiv:1702.00800] [INSPIRE].

[36] A. Kulesza et al., *Associated production of a top quark pair with a heavy electroweak gauge boson at NLO+NNLL accuracy*, *Eur. Phys. J. C* **79** (2019) 249 [arXiv:1812.08622] [INSPIRE].

[37] A. Broggio et al., *Top-quark pair hadroproduction in association with a heavy boson at NLO+NNLL including EW corrections*, *JHEP* **08** (2019) 039 [arXiv:1907.04343] [INSPIRE].

[38] A. Kulesza et al., *Associated top quark pair production with a heavy boson: differential cross sections at NLO+NNLL accuracy*, *Eur. Phys. J. C* **80** (2020) 428 [arXiv:2001.03031] [INSPIRE].

[39] G. Bevilacqua et al., *NLO QCD corrections to full off-shell production of $t\bar{t}Z$ including leptonic decays*, *JHEP* **08** (2022) 060 [arXiv:2203.15688] [INSPIRE].

[40] A. Denner and G. Pelliccioli, *NLO QCD corrections to off-shell $t\bar{t}W^+$ production at the LHC*, *JHEP* **11** (2020) 069 [arXiv:2007.12089] [INSPIRE].

[41] A. Denner and G. Pelliccioli, *Combined NLO EW and QCD corrections to off-shell $t\bar{t}W$ production at the LHC*, *Eur. Phys. J. C* **81** (2021) 354 [arXiv:2102.03246] [INSPIRE].

[42] A. Denner and R. Feger, *NLO QCD corrections to off-shell top-antitop production with leptonic decays in association with a Higgs boson at the LHC*, *JHEP* **11** (2015) 209 [arXiv:1506.07448] [INSPIRE].

[43] A. Denner and M. Pellen, *NLO electroweak corrections to off-shell top-antitop production with leptonic decays at the LHC*, *JHEP* **08** (2016) 155 [arXiv:1607.05571] [INSPIRE].

[44] A. Denner and M. Pellen, *Off-shell production of top-antitop pairs in the lepton+jets channel at NLO QCD*, *JHEP* **02** (2018) 013 [arXiv:1711.10359] [INSPIRE].

[45] A. Denner, J.-N. Lang, M. Pellen and S. Uccirati, *Higgs production in association with off-shell top-antitop pairs at NLO EW and QCD at the LHC*, *JHEP* **02** (2017) 053 [arXiv:1612.07138] [INSPIRE].

[46] S. Actis et al., *Recursive generation of one-loop amplitudes in the Standard Model*, *JHEP* **04** (2013) 037 [arXiv:1211.6316] [INSPIRE].

[47] S. Actis et al., *RECOLA: REcursive Computation of One-Loop Amplitudes*, *Comput. Phys. Commun.* **214** (2017) 140 [arXiv:1605.01090] [INSPIRE].

[48] A. Denner, S. Dittmaier and L. Hofer, *COLLIER: a fortran-based Complex One-Loop LIbrary in Extended Regularizations*, *Comput. Phys. Commun.* **212** (2017) 220 [arXiv:1604.06792] [INSPIRE].

[49] A. Denner and S. Dittmaier, *Reduction of one loop tensor five point integrals*, *Nucl. Phys. B* **658** (2003) 175 [hep-ph/0212259] [INSPIRE].

[50] A. Denner and S. Dittmaier, *Reduction schemes for one-loop tensor integrals*, *Nucl. Phys. B* **734** (2006) 62 [hep-ph/0509141] [INSPIRE].

[51] A. Denner and S. Dittmaier, *Scalar one-loop 4-point integrals*, *Nucl. Phys. B* **844** (2011) 199 [arXiv:1005.2076] [INSPIRE].

[52] R. Frederix, D. Pagani and M. Zaro, *Large NLO corrections in $t\bar{t}W^{\pm}$ and $t\bar{t}t\bar{t}$ hadroproduction from supposedly subleading EW contributions*, *JHEP* **02** (2018) 031 [arXiv:1711.02116] [INSPIRE].

[53] D. Stremmer and M. Worek, *Production and decay of the Higgs boson in association with top quarks*, *JHEP* **02** (2022) 196 [arXiv:2111.01427] [INSPIRE].

[54] S. Catani and M.H. Seymour, *A general algorithm for calculating jet cross-sections in NLO QCD*, *Nucl. Phys. B* **485** (1997) 291 [hep-ph/9605323] [INSPIRE].

[55] S. Dittmaier, *A general approach to photon radiation off fermions*, *Nucl. Phys. B* **565** (2000) 69 [hep-ph/9904440] [INSPIRE].

[56] S. Catani, S. Dittmaier, M.H. Seymour and Z. Trocsanyi, *The dipole formalism for next-to-leading order QCD calculations with massive partons*, *Nucl. Phys. B* **627** (2002) 189 [hep-ph/0201036] [INSPIRE].

[57] S. Dittmaier, A. Kabelschacht and T. Kasprzik, *Polarized QED splittings of massive fermions and dipole subtraction for non-collinear-safe observables*, *Nucl. Phys. B* **800** (2008) 146 [arXiv:0802.1405] [INSPIRE].

[58] A. Denner, S. Dittmaier, M. Roth and D. Wackeroth, *Predictions for all processes $e^+e^- \rightarrow 4$ fermions $+ \gamma$*, *Nucl. Phys. B* **560** (1999) 33 [hep-ph/9904472] [INSPIRE].

[59] A. Denner, S. Dittmaier, M. Roth and L.H. Wieders, *Electroweak corrections to charged-current $e^+e^- \to 4$ fermion processes: Technical details and further results*, *Nucl. Phys. B* **724** (2005) 247 [*Erratum ibid.* **854** (2012) 504] [hep-ph/0505042] [INSPIRE].

[60] A. Denner and S. Dittmaier, *The Complex-mass scheme for perturbative calculations with unstable particles*, *Nucl. Phys. B Proc. Suppl.* **160** (2006) 22 [hep-ph/0605312] [INSPIRE].

[61] A. Denner and S. Dittmaier, *Electroweak Radiative Corrections for Collider Physics*, *Phys. Rept.* **864** (2020) 1 [arXiv:1912.06823] [INSPIRE].

[62] G. Bevilacqua et al., *HELAC-NLO*, *Comput. Phys. Commun.* **184** (2013) 986 [arXiv:1110.1499] [INSPIRE].

[63] PARTICLE DATA GROUP collaboration, *Review of Particle Physics*, *PTEP* **2020** (2020) 083C01 [INSPIRE].

[64] D.Y. Bardin, A. Leike, T. Riemann and M. Sachwitz, *Energy Dependent Width Effects in e^+e^- Annihilation Near the Z Boson Pole*, *Phys. Lett. B* **206** (1988) 539 [INSPIRE].

[65] M. Jeżabek and J.H. Kühn, *QCD Corrections to Semileptonic Decays of Heavy Quarks*, *Nucl. Phys. B* **314** (1989) 1 [INSPIRE].

[66] L. Basso, S. Dittmaier, A. Huss and L. Oggero, *Techniques for the treatment of IR divergences in decay processes at NLO and application to the top-quark decay*, *Eur. Phys. J. C* **76** (2016) 56 [arXiv:1507.04676] [INSPIRE].

[67] A. Denner, S. Dittmaier, M. Roth and D. Wackeroth, *Electroweak radiative corrections to $e^+e^- \to WW \to 4$ fermions in double pole approximation: The RACOONWW approach*, *Nucl. Phys. B* **587** (2000) 67 [hep-ph/0006307] [INSPIRE].

[68] NNPDF collaboration, *Parton distributions for the LHC Run II*, *JHEP* **04** (2015) 040 [arXiv:1410.8849] [INSPIRE].

[69] NNPDF collaboration, *Illuminating the photon content of the proton within a global PDF analysis*, *SciPost Phys.* **5** (2018) 008 [arXiv:1712.07053] [INSPIRE].

[70] A. Buckley et al., *LHAPDF6: parton density access in the LHC precision era*, *Eur. Phys. J. C* **75** (2015) 132 [arXiv:1412.7420] [INSPIRE].

[71] M. Cacciari, G.P. Salam and G. Soyez, *The anti-k_t jet clustering algorithm*, *JHEP* **04** (2008) 063 [arXiv:0802.1189] [INSPIRE].

[72] A. Denner and S. Pozzorini, *One loop leading logarithms in electroweak radiative corrections. 1. Results*, *Eur. Phys. J. C* **18** (2001) 461 [hep-ph/0010201] [INSPIRE].

[73] M. Rubin, G.P. Salam and S. Sapeta, *Giant QCD K-factors beyond NLO*, *JHEP* **09** (2010) 084 [arXiv:1006.2144] [INSPIRE].

[74] D. Pagani, I. Tsinikos and M. Zaro, *The impact of the photon PDF and electroweak corrections on $t\bar{t}$ distributions*, *Eur. Phys. J. C* **76** (2016) 479 [arXiv:1606.01915] [INSPIRE].

[75] A. Denner, S. Dittmaier, S. Kallweit and S. Pozzorini, *NLO QCD corrections to off-shell top-antitop production with leptonic decays at hadron colliders*, *JHEP* **10** (2012) 110 [arXiv:1207.5018] [INSPIRE].